Polarization Entanglement Storage in Ensemble-Based Atomic Memories

by

Bhaskar Mookerji

S.B., Physics, Massachusetts Institute of Technology (2009)

Submitted to the Department of Electrical Engineering and Computer Science
in partial fulfillment of the requirements for the degree of

Master of Engineering and Bachelor of Science in Electrical Engineering and Computer Science

at the

MASSACHUSETTS INSTITUTE OF TECHNOLOGY

June 2011

Author .....
Department of Electrical Engineering and Computer Science
20 May 2011

Certified by .....
Jeffrey H. Shapiro
Director, MIT Research Laboratory of Electronics
Julius A. Stratton Professor of Electrical Engineering
Thesis Supervisor

Accepted by .....
Christopher J. Terman
Senior Thesis Coordinator

Polarization Entanglement Storage in Ensemble-Based Atomic Memories

by

Bhaskar Mookerji

Submitted to the Department of Electrical Engineering and Computer Science
on 20 May 2011, in partial fulfillment of the
requirements for the degree of
Master of Engineering and Bachelor of Science in Electrical Engineering and Computer Science

Abstract

Quantum networks enable the long-distance communication of quantum states through teleportation, but require, in advance, the robust distribution of entanglement between relevant parties. Engineering these networks requires quantum interconnects, which convert quantum states in one physical system to those of another reversibly, and with high fidelity. In this thesis, we describe implementations of long-distance quantum communication networks using polarization entanglement and atomic ensembles. We concisely describe the interactions of a quantum optical field with a heralding atomic ensemble, accounting for multiple-pair events at entanglement generation, as well as finite transmission and photodetection efficiencies under number-resolving and non-resolving photodetection schemes. Using these results, we perform a detailed quantitative performance analysis of quantum networks that distribute and swap entanglement.

Thesis Supervisor: Jeffrey H. Shapiro
Title: Director, MIT Research Laboratory of Electronics
Julius A. Stratton Professor of Electrical Engineering

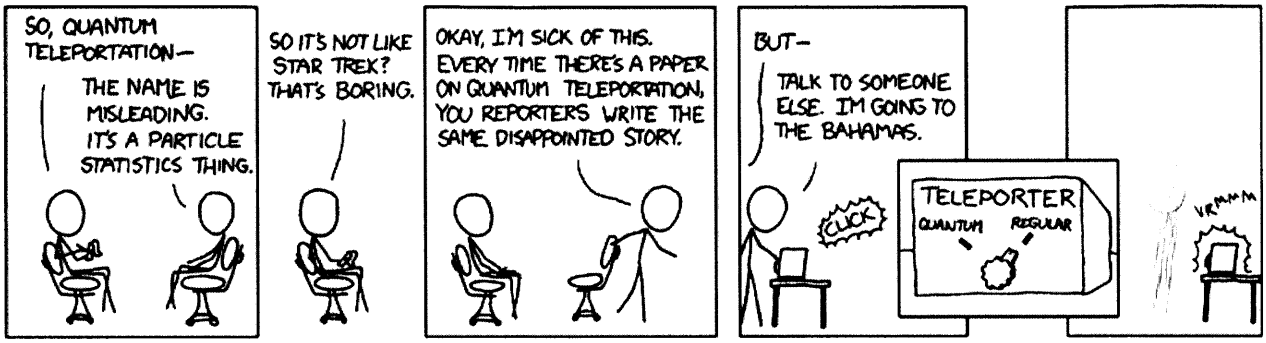

— http://xkcd.com/465/

Acknowledgments

My gratitude for finishing this work goes to Prof. Jeffrey Shapiro, my thesis supervisor and theory principal within the Quantum and Optical Communications Group at the Research Laboratory for Electronics (RLE). In the past year and a half, he has been an extremely accessible, effective advisor, and I have learned a great deal regarding problem-solving intuition and the time management of large theoretical projects.

I am also grateful for generous advice and feedback during the course of this project, particularly with

- Dr. Franco Wong (MIT RLE), Prof. Vladan Vuletic (MIT Physics), and Dr. Zachary Dutton (Raytheon BBN Technologies), for talking to me about the physics of quantum memories, entanglement sources, and atom-photon interactions.

- Prof. Steven Johnson (MIT Mathematics), for discussing with me the mathematics of quantum optics and software engineering issues related to the numerical simulations in this thesis.

- Dr. Ranjith Nair and Dr. Brent J. Yen (MIT RLE), my two office mates, for discussing a wide variety of problems during the course of this work.

Of course, none of this have been possible without the help of my parents, Dipankar and Mallika Mookherji, to whom this thesis is dedicated, and the many friends that make up the greater fabric of my life. This research was funded through the DARPA Quantum Entanglement Science and Technology (QuEST) program.

Contents

List of Figures

List of Tables

Chapter 1

Introduction

Quantum communication exploits quantum mechanical resources, such as entanglement, to achieve tasks unrealizable by classical means, such as accurate teleportation of quantum states and unconditionally secure private key distribution. For such applications, the fundamental problem of quantum communication is the establishment, over optical channels, of entanglement between distant nodes. However, the rate of entanglement distribution to nodes decreases exponentially with channel length. The possibility of creating *scalable* optical quantum networks requires that we overcome this difficulty by storing and processing quantum information locally in quantum memories: first, as repeaters increasing network scalability, and second, as light-matter interfaces to quantum computers [Kim08].

The aim of this thesis is to address the following open problem: the theoretical limits of atomic-ensemble quantum memories that store polarization entanglement. It is part of a larger research program in RLE's Optical and Quantum Communications Group investigating the system performance of ensemble-based hybrid systems in quantum communication. This thesis marries the formalism of collective interactions of atomic ensembles and quantum optical fields with a number-state analysis of our architecture's performance. The remainder of this chapter introduces pre-existing memory and repeater architectures forming the foundation of this work, discusses the importance of polarization entanglement to quantum communication, and outlines the contributions made in this thesis.

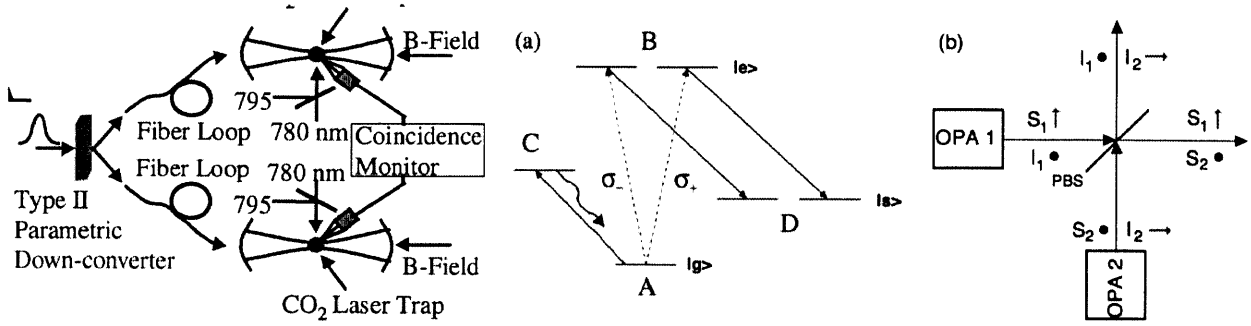

Figure 1-1: Components of a quantum repeater node in the MIT-NU architecture. (a) Parametric downconversion creates pairs of polarization-entangled photons, sending the idler photon to atom-trap 1 and the signal photon to atom-trap 2. Each trap contains a single ultra-cold rubidium atom cooled to its hyperfine ground state. In the energy level diagram, the AB-transition absorbs 795 nm photons, and the BD-transition is coherently driven, thereby enabling storage at D. (b) Polarization-entangled photon pairs generated by a pair of type-II optical parametric amplifiers (OPAs) and a polarizing beam splitter (PBS). The polarizations $\hat{x}$ and $\hat{y}$ are denoted by arrows and bullets, respectively. Figures taken from [LSSH01] and [SW00].

1.1 Architectures for Long-Distance Quantum Networks

An illustration of a model quantum communication system is shown in Fig. 1-1, in the case of a single-trapped atom. Through type-II parametric downconversion, a post-selected maximally-entangled state can be produced of the form,

$$|\psi_1\rangle = \frac{1}{\sqrt{2}} \left(|\sigma_+\rangle_1 |\sigma_-\rangle_2 + e^{i\phi} |\sigma_-\rangle_1 |\sigma_+\rangle_2 \right) \tag{1.1}$$

where σ_+ (σ_-) indicates right (left) circular polarization, and ϕ is a phase offset. An arbitrary polarization of any photon entering the cavity can be stored in the basis of right and left circular polarizations, such that

$$|\psi_2\rangle = \alpha |\sigma_+\rangle + \beta |\sigma_-\rangle . \tag{1.2}$$

Through a Raman Λ-type interaction, a signal or idler photon effectively transfers its entanglement to the degenerate B magnetic hyperfine levels, and subsequently to the D levels through a coherently-driven transition. However, the efficient coupling of a single photon to a single trapped atom is a daunting technical task, requiring that the atom be held in an

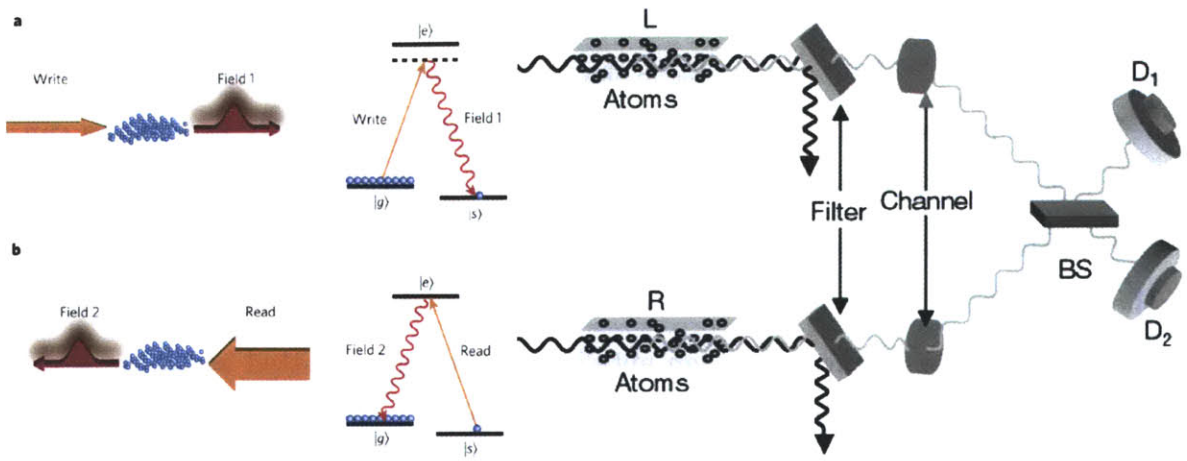

Figure 1-2: Entanglement with the DLCZ protocol. (Left) Weak and strong coherent pulses induce writing and and reading through spontaneous Raman transitions, respectively. (Right) Measurement-induced interference results in a single-excitation entangled state. Figures taken from [Kim08] and [DLCZ01].

ultrahigh-Q cavity. By using an atomic ensemble, we eliminate the need for such a high-quality cavity because a collective atomic state is easily produced by a single photon. Such a state is one in which a single atom has been excited from its ground state $|g\rangle$ at A to the metastable state $|s\rangle$ at D.

To illustrate this behavior for an atomic ensemble, consider N_a atoms prepared in their ground states, a collective state denoted by $|0\rangle_a = |g\rangle^{\otimes N_a}$. Coherently pumping the ensemble creates an inelastic Raman scattering event that is collectively enhanced by constructive interference within the ensemble [Dic54]. The resulting forward-scattered Stokes light arises from coherent spontaneous emission in the ensemble, and the correlated ensemble excitation is a collective spin state,

$$|1\rangle_a = \hat{S}^\dagger |0\rangle_a = \frac{1}{\sqrt{N_a}} \sum_{i=1}^{N_a} |g\rangle_1 \cdots |s\rangle_i \cdots |g\rangle_{N_a} . \tag{1.3}$$

where $\hat{S} = (1/\sqrt{N_a}) \sum_i |g\rangle_i \langle s|$. Because the excitation is composed of many atoms, the collective spin excitation is protected against the loss of individual atoms in the ensemble, increasings its robustness for storage. In the weak interaction limit, in which most of the atoms remain in their ground state, the spin excitation $\hat{S}$ is effectively a ladder operator, as $[\hat{S}, \hat{S}^\dagger] = \sum_i (|g\rangle_i \langle g| - |s\rangle_i \langle s|)/N_a \approx 1$, and the outgoing Stokes light and spin excitation

are in a two-mode squeezed state [DLCZ01]. Generally, the term with the nth atom in $|s\rangle$ acquires the phase $e^{i(\mathbf{k}_w - \mathbf{k}_s)\cdot\mathbf{x}_n}$, where $\mathbf{k}_w$ is the wave vector of pump field, $\mathbf{k}_s$ is that of the detected Stokes photon, and $\mathbf{x}_n$ is the nth atom's position. Collective excitations can be read out very efficiently when converted into single anti-Stokes photons, which are emitted into a well-defined mode because of collective interference. A resonant laser excitation of the collective state in Eqn. 1.3 results in $N_A - 1$ atoms in $|g\rangle$ and one delocalized excitation in $|e\rangle$. Through decay to the $|g\rangle^{\otimes N_a}$, an anti-Stokes photon is emitted along the $|e\rangle - |g\rangle$ transition. Denoting $\mathbf{k}_{as}$ and $\mathbf{k}_r$ as the wave vectors of the anti-Stokes photon and read laser, respectively, satisfying the phase matching condition $\mathbf{k}_s + \mathbf{k}_{as} = \mathbf{k}_r + \mathbf{k}_w$ results in a very high probability amplitude for the anti-Stokes photon to be in the $\mathbf{k}_r + \mathbf{k}_w - \mathbf{k}_s$ direction due to constructive interference [TGS+09].

Our analysis merges the approaches of trapped single atoms in cavity quantum electrodynamics (QED) proposed by MIT and Northwestern University (MIT-NU) and the ensemble-based repeater architecture proposed by Duan, Lukin, Cirac, and Zoller (DLCZ) [LSSH01, DLCZ01]. The MIT-NU and DLCZ protocols both utilize spontaneous Raman transitions to mediate atomic storage. Whereas the MIT-NU protocol has the advantage of storing externally generated entanglement and verifying its success through cycling-transition fluorescence, it is prohibitively difficult to implement because of the strong coupling requirements of cavity QED.

In contrast, the DLCZ protocol creates a collective atomic excitation, as in Eqn. 1.3, not by an external input photon, but by the ensemble itself interacting with a classical (write) field. The entangled state is generated probabilistically (but heralded) through postselection and measurement quantum interference, as shown in Fig. 1-2. In the ideal case of low excitation probability, a photodetection event at either of the two detectors projects the two ensembles into a maximally-entangled singlet state of excitations. Although scalably resilient to issues that might plague such protocols, such as propagation loss and photodetector dark counts, DLCZ requires stable phase coherence and number-resolving photodetectors, neither of which are easy to implement in practice. By enabling the storage of externally-generated entanglement in a DLCZ-type protocol, we will address new error models for entanglement fidelity in quantum memories.

As an aside, it is worth noting a competing approach to photon storage that may serve as a useful comparison in the future, namely, the usage of stimulated Raman transitions and electromagnetically induced transparency (EIT) to increase the coupling of an input quantum field with an atomic ensemble [FL02, Luk03, GAF+07, GALS07]. In this approach, an external coherent control field couples the $|e\rangle - |s\rangle$ transition in a Λ-type atom, adiabatically reducing the group velocity of a single photon wavepacket and trapping it within the ensemble. Such an approach is deterministic, with high throughput, but admits neither easy verification (as in MIT-NU) nor heralding (as in DLCZ). Like the DLCZ protocol above, its compatibility with externally-generated entanglement is an open question.

1.2 Polarization Quantum Entanglement

Because we will be concerned with the behavior of atomic ensembles that are illuminated by the entangled signal and idler produced by optical parametric amplification (OPA), it is important to have an appropriate model for such light beams. As our goal is to quantify the effects of multiple-pair emissions from such a source on the resulting stored entanglement, we cannot immediately default to a postulated biphoton picture. Instead, we shall use the full Gaussian-state description, in which the the input field in this interaction is one of a pair of polarization-entangled light beams generated by the interference of a pair of anti-phased optical parametric amplifiers as shown in Fig. 1-1. We assume that the signal and idler cavities are matched with identical linewidths Γ, and pumping fractions, G^2, of oscillation threshold, with no depletion of or excess noise on the pump [Sha02, SW00]. Following interference, the output fields are in an entangled, zero-mean Gaussian pure state with the normally-ordered and phase-sensitive correlation functions

$$\begin{aligned}
\langle \hat{A}^{\dagger}_{k_j}(t+\tau)\,\hat{A}_{k_j}(t)\rangle &= \frac{G\Gamma}{2}\left[\frac{e^{-(1-G)\Gamma|\tau|}}{1-G} - \frac{e^{-(1+G)\Gamma|\tau|}}{1+G}\right] \\
\langle \hat{A}_{S_j}(t+\tau)\,\hat{A}_{I_j}(t)\rangle &= \frac{(-1)^{j-1}\,G\Gamma}{2}\left[\frac{e^{-(1-G)\Gamma|\tau|}}{1-G} + \frac{e^{-(1+G)\Gamma|\tau|}}{1+G}\right],
\end{aligned} \tag{1.4}$$

where $\{\hat{A}_{k_j}(t)\,e^{-j\omega_k t}:\ k = S\,(\text{signal}), I\,(\text{idler}), j = 1,2\}$ are the positive-frequency, photon-units OPA-output fields. The low-flux output state of this process at a detuning $\Delta\omega$ is given

by expanding out the number ket representations of the OPAs to first order,

$$
\begin{aligned}
|\psi\rangle_{\mathrm{SI}} &= \sum_n \sqrt{\frac{\bar{N}}{\left(\bar{N}+1\right)^{n+1}}}\,|n\rangle_{S_x}|n\rangle_{I_y} \otimes \sum_n (-1)^n \sqrt{\frac{\bar{N}}{\left(\bar{N}+1\right)^{n+1}}}\,|n\rangle_{S_y}|n\rangle_{I_x} \\
&\approx \frac{1}{\bar{N}+1}|0\rangle_{S_x}|0\rangle_{I_y}|0\rangle_{S_y}|0\rangle_{I_x} + \sqrt{\frac{\bar{N}}{\left(\bar{N}+1\right)^3}}\left(|1\rangle_{S_x}|1\rangle_{I_y}|0\rangle_{S_y}|0\rangle_{I_x} - |0\rangle_{S_x}|0\rangle_{I_y}|1\rangle_{S_y}|1\rangle_{I_x}\right) \\
&= |\mathrm{vac}\rangle + \sqrt{\frac{\bar{N}}{\left(\bar{N}+1\right)^3}}\left(|H\rangle_S|V\rangle_I - |V\rangle_S|H\rangle_I\right), \qquad (1.5)
\end{aligned}
$$

where $\bar{N} = 4G^2/\left[(1-G^2-\Delta\omega^2/\Gamma^2)^2 + 4\Delta\omega^2/\Gamma^2\right]$ is the average photon number per mode; and $|H\rangle_S = |1\rangle_{S_x}|0\rangle_{S_y}$, $|V\rangle_S = |0\rangle_{S_x}|1\rangle_{S_y}$, $|H\rangle_I = |1\rangle_{I_x}|0\rangle_{I_y}$, and $|V\rangle_I = |0\rangle_{I_x}|1\rangle_{I_y}$. Following measurement postselection, this state is a maximally entangled singlet state of the form in Eqn. 1.1 [Sha02], and expansions to higher orders account for multiple-pair effects. A useful property of the full state $|\psi\rangle_{\mathrm{SI}}$ is that its anti-normally ordered characteristic function is a zero-mean, jointly Gaussian distribution that remains Gaussian under linear transformations. Its joint density operator is $\hat{\rho}_{SI} = \hat{\rho}_{S_xI_y} \otimes \hat{\rho}_{S_yI_x}$, whose anti-normally ordered characteristic functions are given by

$$
\begin{aligned}
\chi_A^{\rho_{S_xI_y}}(\zeta_S,\zeta_I) &= \langle e^{-\zeta_S^*\hat{a}_{S_x} - \zeta_I^*\hat{a}_{I_y}} e^{\zeta_S\hat{a}^\dagger_{S_x} + \zeta_S\hat{a}^\dagger_{I_y}}\rangle \\
&= e^{-\left(1+\bar{N}\right)\left(|\zeta_S|^2+|\zeta_I|^2\right)+2\bar{N}\mathrm{Re}(\zeta_S\zeta_I)} \qquad (1.6)
\end{aligned}
$$

and

$$
\begin{aligned}
\chi_A^{\rho_{S_yI_x}}(\zeta_S,\zeta_I) &= \langle e^{-\zeta_S^*\hat{a}_{S_y} - \zeta_I^*\hat{a}_{I_x}} e^{\zeta_S\hat{a}^\dagger_{S_y} + \zeta_I\hat{a}^\dagger_{I_x}}\rangle \\
&= e^{-\left(1+\bar{N}\right)\left(|\zeta_S|^2+|\zeta_I|^2\right)-2\bar{N}\mathrm{Re}(\zeta_S\zeta_I)}, \qquad (1.7)
\end{aligned}
$$

which contain all multiple-pair orders of $|\psi\rangle_{\mathrm{SI}}$. Following a linear transformation, the output state $\hat{\rho}_{\mathrm{out}}$ can be determined by taking the inverse Fourier transform of the output characteristic function, with that characteristic function being easily calculated from the input characteristic function and the field transformation. In a memory or teleportation architecture, we want the output—represented by a pure or mixed state $\hat{\rho}_{\mathrm{out}}$— to have the highest

possible fidelity with respect to its input state $\hat{\rho}_{\text{in}}$. The trace separation quantifies this fidelity as $F(\hat{\rho}) = \text{Tr}\left[\sqrt{\hat{\rho}_{\text{out}}}\hat{\rho}_{\text{in}}\sqrt{\hat{\rho}_{\text{out}}}\right]$, which reduces to a projection overlap $\langle\psi_{\text{in}}|\,\hat{\rho}_{\text{out}}\,|\psi_{\text{in}}\rangle$ when the input is the pure state $\hat{\rho}_{\text{in}} = |\psi_{\text{in}}\rangle\langle\psi_{\text{in}}|$.

1.2.1 Entanglement Repeaters and Quantum Teleportation

The most immediate problem affecting the distribution of polarization-entangled photons is photon propagation loss. Although a 1 km length of low-loss, optical telecom fiber ($\lambda = 1.55\ \mu m$)—a relatively short distance—has a transmission nearing 95%, photon transmission decays exponentially with increasing distances, ruling out direct transmission of entangled photons over hundreds of kilometers. In classical communication, this type of signal attenuation is easily compensated with fiber-based amplifiers. However, for quantum communication, the no-cloning theorem prevents noiseless amplification of the non-orthogonal quantum states required for teleportation [WZ82].

Fig. 1-3(a) shows a 'quantum repeater' approach that overcomes the amplifier restriction by incrementally extending entanglement across a larger network [SSdRG09]. Lettered boxes represent memories, and pairs of memories form nodes on the network. For two nodes, A—B and C—D, that are each separately entangled, a joint Bell measurement between memories B and C will entangle systems A and D. This process, known as *entanglement swapping*, establishes entanglement between two networks links that may have never interacted. One can then establish entanglement between memories A and Z that are separated by a distance L by independently creating entanglement at N equally-spaced adjacent nodes out of $2N$ memories. $N-1$ entanglement swapping operations in this network ultimately entangle memories A and Z. For the repeater protocol to work in an asynchronous fashion, these links must be heralding quantum memories.

Once entanglement distribution is successful, we can carry out long-distance quantum communication using teleportation, a protocol described in Fig. 1-3(b). In qubit teleportation, Charlie (C) sends a message (M) to Bob (B) using Alice (A) as an intermediary. Charlie's message is in the form of an arbitrary, unknown qubit spanned by the orthonormal basis $\{|0\rangle, |1\rangle\}$ represented by $|\psi\rangle_C = \alpha|0\rangle_C + \beta|1\rangle_C$, where $|\alpha|^2 + |\beta|^2 = 1$. The steps of the protocol are as follows:

- **Step 1, Entanglement distribution.** An optical source, like that described in Section 1.2, generates polarization-entangled idler and signal photons that are shared and stored by Alice and Bob, respectively. These photons can be any of the four maximally-entangled Bell states,

$$|\psi^{\pm}\rangle_{AB} = \frac{1}{\sqrt{2}}\left(|0\rangle_A|1\rangle_B \pm |1\rangle_A|0\rangle_B\right) \qquad |\phi^{\pm}\rangle_{AB} = \frac{1}{\sqrt{2}}\left(|0\rangle_A|0\rangle_B \pm |1\rangle_A|1\rangle_B\right), \quad (1.8)$$

as long as that state is known to Alice and Bob. In the following, we will assume that Alice and Bob have successfully shared the singlet state $|\psi^-\rangle_{AB}$. The joint state of Alice, Bob, and Charlie form the initial state of the total system:

$$|\psi\rangle_{ABC} = |\psi^-_{AB}\rangle \otimes |\psi_C\rangle = \frac{1}{\sqrt{2}}\left(|0\rangle_A|1\rangle_B - |1\rangle_A|0\rangle_B\right)\left(|\alpha|0\rangle_C + \beta|1\rangle_C\rangle\right). \quad (1.9)$$

- **Steps 2 and 3, Bell measurement and classical communication.** If we define

$$\begin{aligned} |00\rangle_{CA} &= \frac{1}{\sqrt{2}}\left(|\phi^+\rangle_{CA} + |\phi^-\rangle_{CA}\right) & |10\rangle_{CA} &= \frac{1}{\sqrt{2}}\left(|\psi^+\rangle_{CA} - |\psi^-\rangle_{CA}\right) \\ |11\rangle_{CA} &= \frac{1}{\sqrt{2}}\left(|\phi^+\rangle_{CA} - |\phi^-\rangle_{CA}\right) & |01\rangle_{CA} &= \frac{1}{\sqrt{2}}\left(|\psi^+\rangle_{CA} + |\psi^-\rangle_{CA}\right), \end{aligned} \quad (1.10)$$

Eqn. 1.9 can be written in terms of the Bell states as

$$\begin{aligned} |\psi\rangle_{ABC} = &\frac{1}{2}\left[|\psi^+\rangle_{CA}\left(\alpha|1\rangle_B - \beta|0\rangle_B\right) - |\psi^-\rangle_{CA}\left(\alpha|1\rangle_B + \beta|0\rangle_B\right)\right] \\ &+ \frac{1}{2}\left[|\phi^-\rangle_{CA}\left(\beta|0\rangle_B + \alpha|1\rangle_B\right) + |\phi^+\rangle_{CA}\left(\beta|0\rangle_B - \alpha|1\rangle_B\right)\right]. \end{aligned} \quad (1.11)$$

Alice performs a joint measurement on her idler photon and the message qubit entrusted to her by Charlie, projecting Bob's state into one of four single-qubit rotations of Charlie's initial state. Alice sends her measurement result—one of 00, 01, 10, or 11—to Bob over a classical communications channel. Charlie's qubit is destroyed in this measurement process.

- **Step 4, State transformation.** Bob receives Alice's measurement data and performs the appropriate single-qubit rotation on his signal photon using waveplates to

recover Charlie's state. Because Alice's measurement outcomes are all equally likely, the teleportation reveals no information about Charlie's initial state.

Together, entanglement repeaters and teleportation form basis for high-fidelity communications of quantum states over long distances.

1.3 Overview and Goals

Using Gaussian-state outputs from the OPA's, we can quantify fidelity loss in entanglement distribution by accounting for multiple-pair effects, fiber propagation loss, photodetection limitations, and phase mismatch between atomic ensembles. A Gaussian-state analysis for finite atomic ensembles, while valid for the DLCZ protocol, is not applicable for the distribution of externally-generated entanglement. The discussion in this thesis focuses on building a new abstraction for quantum memories and a corresponding formalism for its architectural analysis.

The remainder of the thesis is organized as follows:

- **Chapter 2** summarizes the atomic physics concerning the interactions between multi-atom ensembles and quantized light fields. Sections 2.1 and 2.2 formally introduce quantized fields and common assumptions regarding their interactions with collective atomic states, particularly in the context of three-level Raman interactions. In Section 2.3, we apply this formalism to derive the trilinear Hamiltonian describing a heralding DLCZ-type memory.

- **Chapter 3** synthesizes the primary theoretical results of this thesis: an architectural analysis of a DLCZ-type quantum communication system, driven by a dual-OPA source, with particular emphasis paid to multiple-pair effects. In Section 3.1, we provide an overview of this architecture and discuss relevant experimental parameters for a prototype system. Assuming perfect absorption by the memories, we determine the fidelity and success probability of our heralding architecture in Section 3.2 by applying a number-state analysis. Section 3.3 applies a Gaussian state analysis to polarization entanglement connection.

- **Chapter 4** summarizes our theoretical results and discusses possible future directions for studying architectures for quantum communication with polarization entanglement.

- **Appendix A** presents a Quantum Monte Carlo simulation of the pump, signal, and idler modes of a trilinear Hamiltonian. We'll use this simulation to: (i) justify an *ansatz* solution in the Chapter 3's number-state analysis; and (ii) explain why approximate solutions in the literature fail to adequately describe memory-loading dynamics. Section A.1 argues that trilinear Hamiltonians are not analytically diagonizable using a finite Lie group representation. Section A.2 lists the code for the numerical simulation of the trilinear Hamiltonian's associated master equation.

1.4 Notation and Abbreviations

Table 1.1 summarizes symbols and abbreviations common throughout this thesis.

Symbol/Abbreviation	Definition
Symbols	
$\hat{a}$, $\hat{b}$, $\hat{S}$	Pump, heralding, and spin excitation operators
$\|g\rangle$, $\|e\rangle$, $\|s\rangle$	Ground, excited, and metastable atomic states
N_a	Number of neutral atoms in atomic ensemble
g_c, κ	Cavity mode coupling strength and decay rate
Ω, Δ	Rabi frequency and excited-state detuning
$\bar{N}$	Average photon number per mode
$f_{n,m}\left(\bar{N}\right)$	Dual-OPA thermal coefficient
η	Beam splitter transmission efficiency
$\hat{B}$	Beam splitter operator
$B_{N_1,N_2}^{n_1,n_2}\left(\eta,\phi_t,\phi_r\right)$	Beam splitter coefficient relating n_1+n_2 input photons to N_1+N_2 output photons
Abbreviations	
DLCZ	Duan-Lukin-Cirac-Zoller (Protocol)
MIT-NU	MIT-Northeastern University (Protocol)
PNRD	Photon-number resolving detection
NRPD	Non-resolving photon detection
POVM	Positive operator valued measure
OPA	Optical parametric amplifier
SPDC	Spontaneous parametric down conversion
NPBS/PBS	(Non-)Polarizing beam splitter
QWP/HWP	Quarter/Half-wave plate
h.c.	Hermitian conjugate (adjoint)

Table 1.1: Common symbols and abbreviations employed in this thesis.

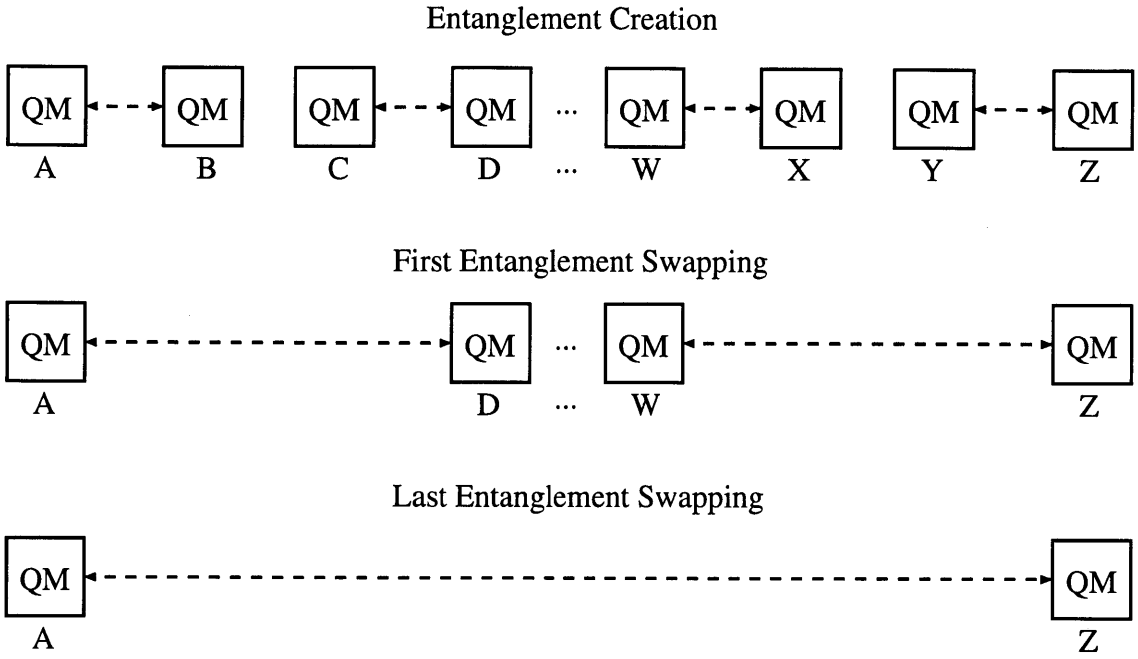

(a) Principle of a quantum repeater architecture. Entanglement is independently created at short distances between nodes AB...YZ. Entanglement is swapped between neighboring links such that locations A and D, for example, share entanglement over an intermediate distance. Swapping occurs over successively larger distances until links at the desired separation, A and Z, are entangled. Figure based on [SSdRG09].

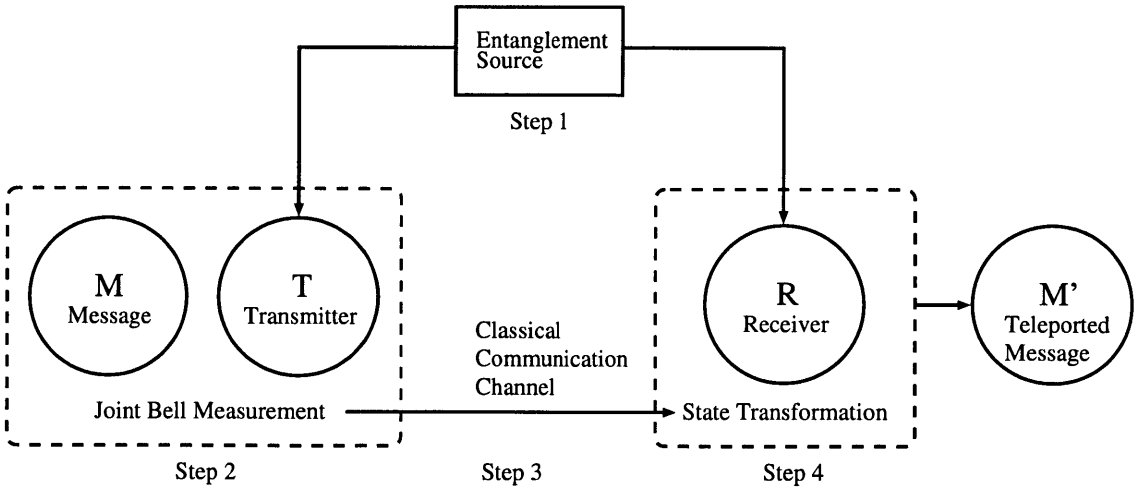

(b) Optical qubit teleportation. Two nodes sharing entanglement can teleport a qubit using local Bell measurements and a classical communication channel. Figure based on [Sha08].

Figure 1-3: Fundamentals of quantum communication using entanglement connection and teleportation.

Chapter 2

Quantum Memories and Repeaters using Fundamental Light-Matter Interactions

Photons interact very weakly with their environment and undergo minimal quantum state decoherence, making them robust carriers of quantum information over reasonable distances. These strengths in passive communication are quite problematic, however, when building larger networks, as photons are very difficult to localize and store. In the following, we will discuss the finer details of modeling the coherent transfer of quantum states of light to atomic ensembles, particularly conditions for strong Raman interaction and unity absorption of photons by optically thick atomic gases. This treatment places an emphasis on underlying physical assumptions required for operating such memories.

2.1 Describing Light and Atomic Fields

In this section, we introduce boson excitation representations of electromagnetic fields and atomic spin, and some important underlying assumptions and approximations relevant for describing their interactions in Section 2.2. We consider an ensemble of N_A Λ-type atoms confined in a single-sided, ring cavity, as shown in Fig. 2-1. The $|g\rangle - |e\rangle$ and $|e\rangle - |s\rangle$ transitions are coupled to the cavity-modes $\hat{a}$ and $\hat{b}$ with coupling coefficient g_{ge} and g_{es},

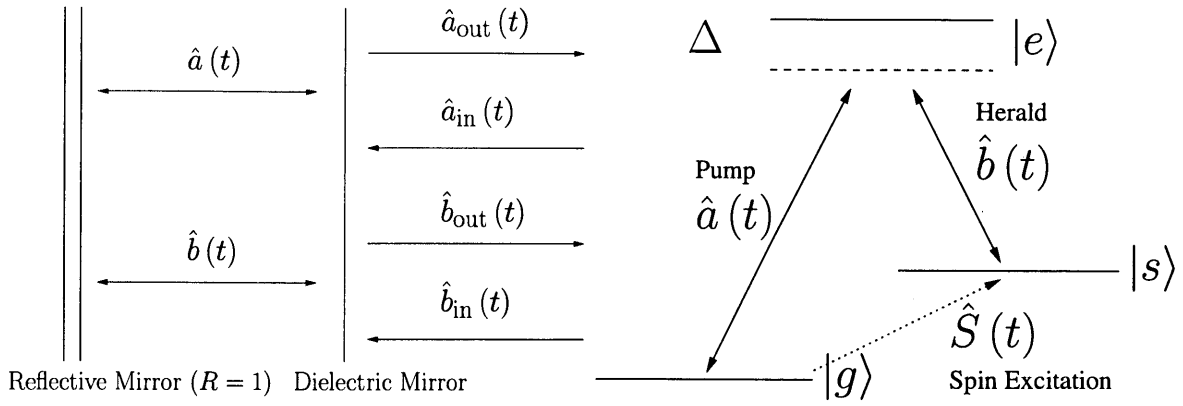

Figure 2-1: DLCZ with quantum field inputs. (Left) Input-output formalism for a single-sided, two-mode ring cavity. (Right) Interaction in a three-mode parametric amplifier

respectively. For reasons discussed in Section 2.2, the two cavity-mode fields have a frequency detuning Δ from the excited state $|s\rangle$. Because the algebra describing the interactions of three boson operators is quite complicated, we will have to simplify this calculation. We start by assuming that the $|g\rangle - |e\rangle$ transition is coupled to a classical field, as in the DLCZ case, and then replace the classical Rabi frequency term in the resulting interaction Hamiltonian with a quantized field term. This derivation is partially based on the discussion by Hammerer and Polzik in [HSP10], although similar and less-detailed discussions can be found other quantum optics texts [Ste10].

A monochromatic, quantized, paraxial electromagnetic field propagating nominally in the **z**-direction through vacuum is represented by

$$\hat{\mathbf{E}}(\vec{r},t) = \sqrt{\frac{2\pi\omega}{c}} \sum_{m\sigma} \mathbf{e}_{\omega} u_m(\mathbf{r}_{\perp}; z)\, e^{i(k_m z - \omega t)} \hat{a}_{m\sigma}(z) + \text{h.c.}, \tag{2.1}$$

where $\mathbf{e}_{\sigma}$ is the polarization vector (labeled by σ) and k_m is the longitudinal wave number. The mode functions $\{u_m(\mathbf{r}_{\perp}; z)\}$ characterize the transverse profile of the field and form a complete orthogonal basis in the plane defined by $\mathbf{r}_{\perp}$. The first and second terms of this field are also denoted later as the positive ($\hat{\mathbf{E}}^{(+)}$) and negative ($\hat{\mathbf{E}}^{(-)}$) frequency fields, respectively. In defining the field annihilation operator $\hat{a}_{m\sigma}$, we make a *dipole approximation* (also known as a *long-wavelength approximation*), that assumes that the wavelength of the field is much longer than the effective size of the atomic ensemble, thereby neglecting variations of the field

over the atoms' extent[1]. For this approximation to be valid in the case of a pencil-shaped atomic ensemble of length L_a, the wave vectors of the pump and herald fields must satisfy $(k_a - k_b) L_a \ll \pi$ [DLCZ01]. The position-space annihilation operator in Eqn. 2.1 has the commutator

$$\left[\hat{a}_{m\sigma}(z), \hat{a}^{\dagger}_{m\sigma}(z')\right] = c\delta_{m,m'}\delta_{\sigma,\sigma'}\delta(z - z'). \tag{2.2}$$

The normalization c is chosen such that the traveling wave fields $\hat{a}_{m\sigma}(z,t)$ have the appropriate free-space commutator. Further details regarding the slowly-varying annihilation operator are given in [HSP10].

The populations of the two ground states $|g\rangle$ and $|s\rangle$ are described by angular momentum operators acting on the mth atom,

$$\hat{\sigma}_{x,m} = \frac{1}{2}\left(|g\rangle_m \langle g| - |s\rangle_m \langle s|\right) \quad \hat{\sigma}_{y,m} = \frac{1}{2}\left(|g\rangle_m \langle s| + |s\rangle_m \langle g|\right) \quad \hat{\sigma}_{z,m} = \frac{1}{2i}\left(|g\rangle_m \langle s| - |s\rangle_m \langle g|\right) \tag{2.3}$$

and the atomic lowering operator,

$$\hat{\sigma}_{+,m} = \hat{\sigma}_{y,m} + i\hat{\sigma}_{z,m} = |g\rangle_m \langle s|, \tag{2.4}$$

where x is the quantization axis chosen by convention. The collective angular momentum operators are then $\hat{S}_i = \sum_j \hat{\sigma}_{i,j}$ $(i = x, y, z)$ and $\hat{S}^2 = \hat{S}_x^2 + \hat{S}_y^2 + \hat{S}_z^2$, which obey the standard angular momentum commutators $\left[\hat{S}_i, \hat{S}_j\right] = i\epsilon_{ijk}\hat{S}_k$ and $\left[\hat{S}_i, \hat{S}^2\right] = 0$, respectively. The collective states are specified uniquely by the angular momentum states $|s, m_x\rangle$, where s is the total angular momentum quantum number specified by $\hat{S}^2$, and m_z is the x-axis angular momentum quantum number specified by $\hat{S}_x$. The ensemble state where all the atoms are in the ground state $|g\rangle$ is labeled by the corresponding angular momentum state $|s = N_A/2, m_x = N_A/2\rangle$. For $N_A \gg 1$ and small perturbations to the ensemble, $\hat{S}_x$ can be approximated by its expectation value $\langle \hat{S}_x \rangle$, which is $N_A/2$ for the collective ground state.

[1]With this assumption, the light-ensemble interaction Hamiltonian is simply a dot product between the quantized field operator (Eqn. 2.1) and the atomic dipole operator (Eqn. 2.9), as shown in Eqn. 2.8.

By defining canonical position and momentum operators,

$$\hat{X}_A = \frac{\hat{S}_y}{\langle \hat{S}_x \rangle} \qquad \hat{P}_A = \frac{\hat{S}_z}{\langle \hat{S}_x \rangle}, \tag{2.5}$$

the normalized, collective annihilation operator is,

$$\hat{S} = \frac{\hat{X}_A + i\hat{P}_A}{\sqrt{2}} = \frac{1}{\sqrt{\langle \hat{S}_x \rangle}} \sum_m \hat{\sigma}_{+,m} = \frac{1}{\sqrt{\langle \hat{S}_x \rangle}} \sum_m |g\rangle_m \langle s|, \tag{2.6}$$

whose action is consistent with Eqn. 1.3.

2.2 Collective Atom-Field Interactions

In the following, we will first consider an interaction with a single atom at location $\mathbf{r}$, extend the result to the entire ensemble, and show that parametric amplification occurs between the heralding and spin modes. The total Hamiltonian describing the optical fields, the atoms, and their interaction is

$$\hat{H} = \hat{H}_A + \hat{H}_F + \hat{H}_{\text{int}}. \tag{2.7}$$

The atoms' stable ground states are denoted by $|g_m\rangle$ and their excited states by $|e_m\rangle$. The atomic and optical Hamiltonians are $\hat{H}_A = \sum_m \omega_0 |e_m\rangle \langle e_m|$ and $\hat{H}_F = \sum_m \omega \hat{a}_m^\dagger \hat{a}_m$, respectively. With the dipole approximation, the atom-field interaction Hamiltonian is

$$\hat{H}_{\text{int}} = -\hat{\mathbf{d}} \cdot \hat{\mathbf{E}}, \tag{2.8}$$

where $\hat{\mathbf{d}}$ is the atomic dipole operator $\hat{\mathbf{d}} = -q\mathbf{r}_e$, as a function of electronic charge $q = -e$ and the atomic electron position $\mathbf{r}_e$. The dipole operator governs the transitions between states, and it can be shown that for magnetic hyperfine states $\{|g_m\rangle\}$ and $\{|e_m\rangle\}$, all matrix elements $\langle g_m | \mathbf{d} | g_{m'} \rangle$ and $\langle e_m | \mathbf{d} | e_{m'} \rangle$ of the dipole operator vanish. For a single atom, we get

$$\hat{\mathbf{d}} = \langle g | \hat{\mathbf{d}} | e \rangle (\hat{\sigma}_+ + \hat{\sigma}_-) = \hat{\mathbf{d}}^{(+)} + \hat{\mathbf{d}}^{(-)}, \tag{2.9}$$

with positive and negative frequency components defined similarly to Eqn 2.1. Expanding out the dipole and field operators, the interaction Hamiltonian simplifies to

$$\begin{aligned}\hat{H}_{\text{int}} &= -\left(\hat{\mathbf{d}}^{(+)} + \hat{\mathbf{d}}^{(-)}\right) \cdot \left(\hat{\mathbf{E}}^{(+)} + \hat{\mathbf{E}}^{(-)}\right) \\ &= -\hat{\mathbf{d}}^{(-)} \cdot \hat{\mathbf{E}}^{(-)} - \hat{\mathbf{d}}^{(+)} \cdot \hat{\mathbf{E}}^{(+)} - \hat{\mathbf{d}}^{(+)} \cdot \hat{\mathbf{E}}^{(-)} - \hat{\mathbf{d}}^{(-)} \cdot \hat{\mathbf{E}}^{(+)} \\ &\approx -\hat{\mathbf{d}}^{(+)} \cdot \hat{\mathbf{E}}^{(-)} - \hat{\mathbf{d}}^{(-)} \cdot \hat{\mathbf{E}}^{(+)} \end{aligned} \tag{2.10}$$

under the *rotating wave approximation.* This approximation leverages the relative time scales of dynamics under unitary time evolution. Recalling the time dependencies $\mathbf{d}^{(\pm)} \sim e^{\mp i\omega_0 t}$ and $\mathbf{E}^{(\pm)} \sim e^{\mp i\omega t}$, the first two like-sign operator products oscillate quickly at $e^{\pm i(\omega+\omega_0)t}$, while the cross-sign operator products oscillate slowly at $e^{\pm i(\omega-\omega_0)t}$. With $|\omega - \omega_0| \ll |\omega + \omega_0|$, we can focus on relatively slow dynamics by assuming that the fast terms have zero average value and dropping those products. Note that transformation to the rotating frame, with respect to the incoming optical frequency, changes the free atomic Hamiltonian in Eqn. 2.7 to $\hat{H}_A = \sum_m \Delta_m |e_m\rangle \langle e_m|$, where Δ_m is the detuning of the mth excited state with respect to the pump laser frequency ω.

The detuning of the optical fields from ω_0 allows us to *adiabatically eliminate* the excited state from our later analysis. Expanding out Eqn. 2.10 by its matrix elements gives

$$\hat{H}_{\text{int}} = -\sum_{m,m'} \hat{\mathbf{E}}^{(-)} \cdot \hat{\mathbf{d}}^{(+)}_{m,m'} |g_m\rangle \langle e_{m'}| + \text{h.c.}. \tag{2.11}$$

With the atomic free evolution and the interaction Hamiltonian taken together, the time evolution of these matrix elements is given by

$$\frac{d}{dt} |g_m\rangle \langle e_{m'}| = -i\Delta_{m'} |g_m\rangle \langle e_{m'}| + i\hat{\mathbf{E}}^{(+)} \cdot \sum_{m''} \left(\hat{\mathbf{d}}^{(-)}_{m',m''} |g_m\rangle \langle g_{m''}| - \hat{\mathbf{d}}^{(-)}_{m'',m'} |e_{m''}\rangle \langle e_{m'}|\right). \tag{2.12}$$

Here we can drop two more terms: first, for weak excitations, we can eliminate the excited-state operator $|e_{m''}\rangle \langle e_{m'}|$, and second, provided that $\hat{\mathbf{E}}^{(+)} \cdot \hat{\mathbf{d}}^{(-)}_{m,m'} \ll \Delta_{m'}$, we can eliminate the left-hand time derivative because its dynamics are slow relative to time-evolution at the detuning $\Delta_{m'}$. Under this adiabatic approximation, the matrix elements of the Hamiltonian

are

$$|g_m\rangle\langle e_{m''}| \approx \sum_{m''} \frac{\hat{\mathbf{E}}^{(+)}(\mathbf{r}) \cdot \hat{\mathbf{d}}^{(-)}_{m',m''}}{\Delta_{m'}} |g_m\rangle\langle g_{m''}| . \tag{2.13}$$

With the rotating-wave and adiabatic approximations, we determine the effective ground state Hamiltonian $\hat{H}'_{\text{int}}$ by substituting Eqn. 2.13 into Eqn. 2.11 and simplifying. The effective ground state Hamiltonian is then

$$\hat{H}'_{\text{int}} = -\sum_{m,m',m''} \frac{\left(\hat{\mathbf{E}}^{(-)}(\mathbf{r}) \cdot \hat{\mathbf{d}}^{(+)}_{m',m''}\right)\left(\hat{\mathbf{d}}^{(-)}_{m'',m'} \cdot \hat{\mathbf{E}}^{(+)}(\mathbf{r})\right)}{\Delta_{m''}} |g_{m'}\rangle\langle g_m| . \tag{2.14}$$

In describing the interaction between a quantum field, a classical field, and the entire ensemble, we integrate over Eqn. 2.14 for all atoms in space and apply the quantized electric field given in Eqn. 2.1. Assuming that the classical and quantum fields are co-propagating in the **z** direction, it can be shown that resulting Hamiltonian is

$$\hat{H} = \int dz \left[\frac{|\Omega(z,t)|^2}{4\Delta}\hat{S}^\dagger(z)\hat{S}(z) - \left(\frac{g^*(z)\Omega(z,t)}{2\Delta}\hat{b}^\dagger(z)\hat{S}^\dagger(z) + \text{h.c.}\right)\right], \tag{2.15}$$

where $\hat{b}$ is the heralding field operator as included in Eqn. 2.1, and the coupling constant $g(z)$ and Rabi frequency $\Omega(z,t)$ are,

$$g(z) = \sqrt{\frac{2\pi\omega n(z)}{c}}\hat{\mathbf{d}}^{(-)}_{es} \cdot \vec{\mathbf{e}}_q \qquad \Omega(z,t) = 2\hat{\mathbf{d}}^{(-)}_{eg} \cdot \langle\hat{\mathbf{E}}^{(+)}\rangle e^{-i(k_0 z - \omega_0 t)}, \tag{2.16}$$

where $n(z)$ is the density distribution of the ensemble, $\vec{\mathbf{e}}_q$ is the polarization of the quantized field, and the dot product terms describe the atom-light field overlap [HSP10]. The first term of the Hamiltonian describes the level shift of the ground state in the presence the classical pump field (the ac Stark effect), the second term describes the parametric interaction between the heralding optical field and the collective ensemble excitation. This is consistent with the heralding photon and spin wave parametric amplification described in the original DLCZ protocol, up to a scale factor in the interaction strength [DLCZ01]. For abstracting the behavior in quantum memories, it sufficient to omit the sum over multiple modes and the integration over **z** by incorporating collective enhancement into the coupling term such that

$g \rightarrow g\sqrt{N_a}$. Replacing the strong classical field Rabi frequency Ω with a quantized pump field $g_{ge}\hat{a}$ yields a trilinear Hamiltonian describing the effective interaction been quantized pump, spin wave, and heralding modes:

$$\hat{H}_{\text{int}} = \frac{|g_{es}g_{ge}|\, N_a}{\Delta}\left(\hat{a}\hat{b}^{\dagger}\hat{S}^{\dagger} + \hat{S}\hat{b}\hat{a}^{\dagger}\right). \tag{2.17}$$

In Chapter 3, we assume an *anzatz* solution such that N entangled photons are absorbed by an ensemble memory and are converted, without loss, to N spin excitations and N heralding photons. Justifications for this assumption are provided in Appendix A using the algebraic symmetries of Eqn. 2.17 and a numerical simulation, respectively. Note that that operations preserving the Gaussian properties of a quantum state's Wigner function (e.g., for polarization-entangled light) must be quadratic in its boson operator terms [BvL05]. Any quadratic interaction Hamiltonian is thus a Gaussian operation, and the solutions for its input-output behavior is a Bogoliubov transformation of the input modes. However, it is not even possible to determine the analytical dynamics for Eqn. 2.17, because it is not a quadratic Hamiltonian. In the following section, we will describe some subtleties and prospects for achieving strong interactions between quantized excitations, in the trilinear case.

2.3 Engineering Quantized Field Absorption

The interaction strength in Eqn. 2.17 includes an inverse dependence on the detuning from the excited state energy, and a direct dependence coupling coefficients between the cavity fields and the ensemble. Under what conditions is it possible to make a heralding memory for a quantum field near-unity efficient?

Although reducing the detuning Δ of the input field increases interaction strength, it also has the adverse effect of moving the memory's operating regime out of Raman scattering and into fluorescence, in which the ensemble experiences inhomogeneous broadening between the ground and excited states, thereby eliminating the intra-ensemble quantum interference required in the DLCZ protocol. The derivation of the parametric Hamiltonian (Eqn. 2.15) in

Section 2.2 assumed an adiabatic approximation with a very large detuning. In our ensemble, we will have to assume a homogenous distribution of atoms coincident with the write field, as atoms closer to resonance with the write field will have a larger amplitude of emitting a heralding photon. Near-resonant excitation of the excited state impart phases differing from atom to atom in an inhomogeneous ensemble. Ottaviani, et al. have characterized the collective atomic character of near-resonance or inhomogeneously broadened ensembles (i.e., Doppler broadening) [OSdR$^+$09], whose results are summarized in Fig. 2.3. They assume an ensemble with inhomogeneous broadening of 0.5 GHz and a Gaussian temporal pulse shape for the input centered at 0.2 μs with a duration specified by a full-width half maximum at 0.1 μs. The collectivity is defined as the fidelity of an ideal Dicke state against that produced by a near-resonance input field. Figures 2-2(a) and 2-2(b) show that collectivity decreases significantly for resonant pulses, but is almost unity for the pulse duration using detuning only twice the inhomogeneous broadening. Collectivity is enhanced by spontaneous broadening, which suppresses fluorescent heralding after the pulse, but undergoes decay through spin decoherence. Furthermore, the heralding probability closely follows the pulse shape of the input field when it is off-resonance. For larger detunings, a much broader frequency class of atoms in the ensemble contribute to the heralding photon, as shown in Fig. 2-2(c).

We can compensate for finite detunings and heralding probabilities in these ensembles by increasing the ensemble's optical depth, which is limited in free-space interactions by ensemble size and coupling strength. Several approaches use multi-pass optical cavities to increase the likelihood of a successful Raman scattering event between a cavity field and the enclosed ensemble [JDB$^+$04, BTVac05, SdRA$^+$07, TSLVac06, STTVac07]. The cavity-ensemble heralding efficiency is captured by the cooperativity parameter $C = g_c^2 N_A / \kappa_c \gamma$, where g_c is the single-atom coupling constant to the cavity mode, κ_c is the cavity decay rate, and γ is the excited state spontaneous decay rate. It can be shown that the cooperativity is approximately $C \sim fd$, where d is the optical depth of the ensemble and the finesse f is approximately the number of passes the optical field makes in the cavity. Optical cavities are used in the magnon-type memory (Fig. 2-3), in which a single collective excitation is shared between between two spatially-overlapping atomic ensembles [TGS$^+$09]. Photons of

arbitrary polarization states are stored between two ensembles that absorb only left- (σ^+) and right-circularly (σ^-) polarized light, respectively, and emit only linearly (π) polarized light into the cavity resonator, thereby eliminating any which-path information. The memory itself is an ensemble of approximately 8000 cesium atoms loaded from a far-detuned magneto optical trap (MOT) into a one-dimensional optical lattice overlapping a medium-finesse ($f = 140$) optical cavity. A spatially homogenous, DC magnetic field allows time-dependent control of polarization storage through Larmor precession of the ensembles magnetic moment. In theory, single-photon conversion efficiencies for this type of magnon memory are quite high. It was also shown in Section 2.2 and Appendix A that a heralding quantum memory operating with a single- or few-photon pump field performs a 'non-Gaussian' operation because of its Hamiltonian's (Eqn. 2.17) algebraic symmetries. Several approaches exist for enhancing nonlinear optical effects between optical and ensemble excitations, such as optically imprinted Bragg mirrors ([AL02, BZL03]), interactions between ensembles of atoms in optical lattices ([MdVPC08]), and atomic blockades using Rydberg-level atoms ([LFC+01]).

Bandwidth requirements for atomic ensembles impose restrictions on the phase matching bandwidth of our polarization-entanglement source. In Section 1.2, we introduced OPA sources for polarization entanglement. To be compatible with ensemble-based quantum memories and enable efficient quantum state transfer, the signal and idler output fields must be nearly-resonant with the center frequency of the desired atomic transition and have a narrow spectral bandwidth—anywhere between 10 and 100 MHz—matching that of the ensemble [SSdRG09].

There are two techniques for reducing the spectral bandwidth of the output from spontaneous parametric down conversion. The first is cavity-enhanced down conversion, in which a nonlinear crystal in a cavity will only emit light in prescribed cavity modes. Because cavity output is spectrally multimode, a Fabry-Perot etalon or filter cavity is required to select a single cavity mode [KWS06, SKB09]. Recently, groups have created type-II polarization entanglement sources compatible with alkali-gas ensembles of rubidium and cesium by applying spectral filtering and frequency locking, resulting in bandwidths of 2.7 MHz and 9.6 MHz, and corresponding spectral brightnesses of approximately 330 and 6 entangled pairs per second per mW of pump power per MHz of output bandwidth [SKUB09, BQY+08].

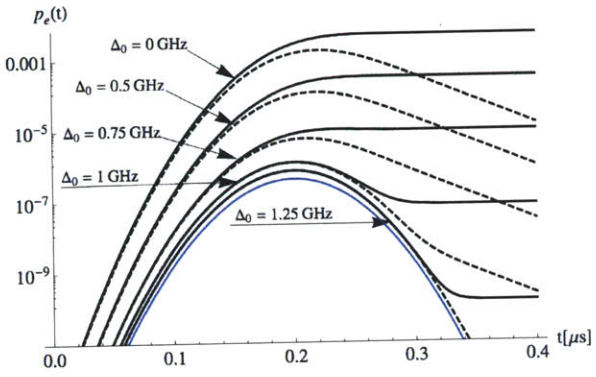

(a) Mean excited state population $p_e(t)$.

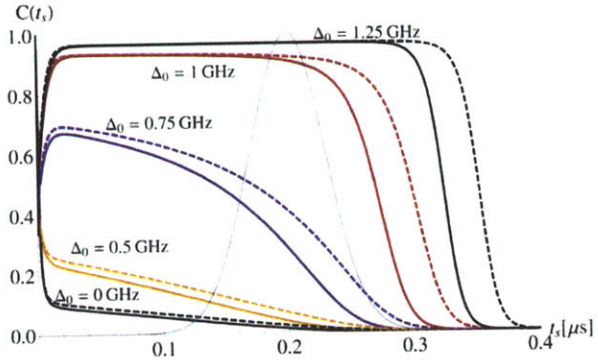

(b) Collectivity of an atomic excitation as a function of time of Stokes photon emission t_s.

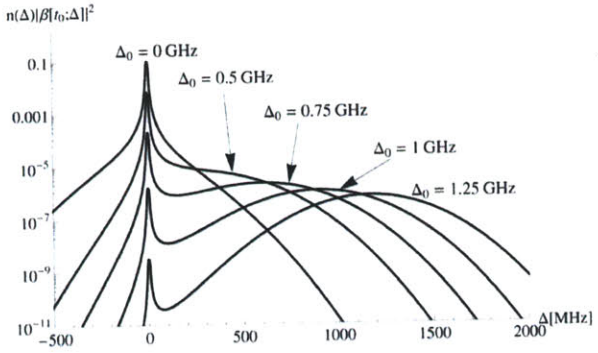

(c) Contributions of atomic frequencies to collective atomic excitation and Stokes photon emission. Contributions from the collective atomic distribution dominate resonant fluorescence at higher detunings.

Figure 2-2: Contributions of resonance fluorescent absorption and Raman scattering to the collectivity of a Dicke excitation. The calculations assume that the excited-state energies of the atoms are Gaussian-distributed about some center frequency. All quantities are plotted for different detunings Δ_0 from that center frequency. In Figures 2-2(a) and 2-2(b), dashed lines include spontaneous emission broadening $\Gamma = 5$MHz and the fine blue line denotes the squared Rabi frequency $\Omega^2(t)$ of the pump laser. Figures are taken from [OSdR+09].

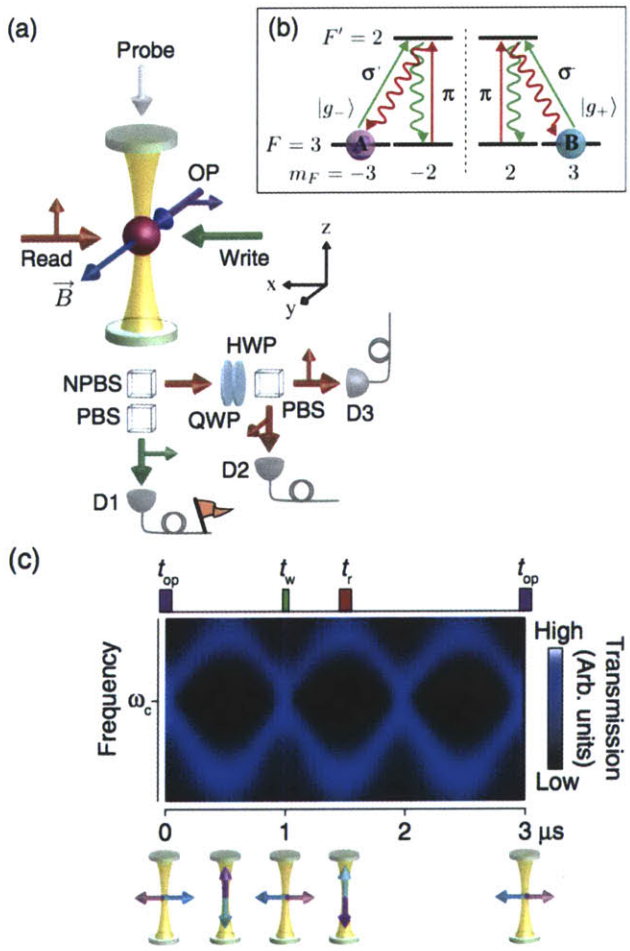

Figure 2-3: Operation of a magnon-type quantum memory. (a) Read/Write Control. Arrows indicate polarization vector. A static magnetic field induces Larmor precession, and the optical pump (OP) controls the atomic ground state and write/read processes. (b) Atomic energy levels. Ensembles A and B are prepared in a hyperfine ground state. The write (green) and read (red) processes are $\sigma^{\pm} - \pi$ and $\pi - \sigma^{\pm}$ spontaneous Raman transitions, respectively. (c) Ensemble Larmor Precession. The ensemble precession is quantified by measured cavity transmission. Times for optical pumping (t_{op}), write (t_w), and read (t_r) processes are labeled accordingly. Figures are taken from [STTVac07].

Chapter 3

Heralded Polarization Entanglement Distribution with Atomic Ensembles

This chapter combines the operating principles of ensemble-based quantum memories, as described in Chapter 2, with architectures for polarization entanglement distribution, entanglement connection, and quantum teleportation. We will first discuss our architecture for entanglement distribution and provide a very basic abstraction for quantum memories. The remainder characterizes figures of merit—fidelity, heralding probability, and protocol success probability—under various transmission loss and photodetection conditions.

3.1 Architecture Overview

We will first discuss our overall architecture and loss model, followed by particular details of a dual-OPA polarization entanglement source and quantum memories. Our architecture for polarization entanglement distribution, shown in Fig. 3-1, is a modification of the standard DLCZ architecture shown in Fig. 1-2. In the original DLCZ protocol, both ensembles are coherently pumped and the probability that both ensembles will emit single photons is low compared to that for emission from a single ensemble. Interference at the 50-50 beam splitter in Fig. 1-2 erases any which-path information for the emission event, so a single detection at either photon counter D_1 or D_2 is used to herald entanglement of the two ensembles. The ideal situation in Fig. 3-1 is when a polarization singlet is emitted from the source and the

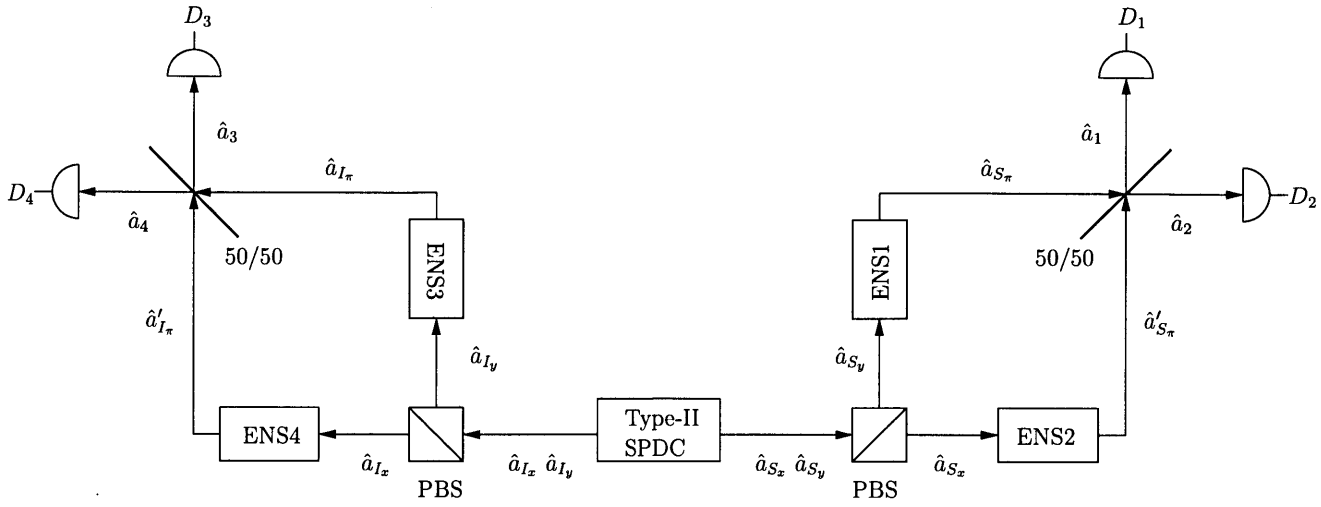

Figure 3-1: Modified DLCZ architecture for distributing polarization entanglement, using a spontaneous parametric downconversion (SPDC) source and interferometer measurement for entanglement verification.

overall system is lossless. The polarizing beam splitters (PBS) then load the signal and idler photons from the singlet into a coherent superposition of excitations of ensembles 1 and 2 and ensembles 3 and 4, respectively. This loading is heralded by the single-photon detections from pair (D_1, D_2) and (D_3, D_4).

Fig. 3-2 encompasses the error modes for the Fig. 3-1 distribution architecture. The Type-II SPDC source may produce multiple signal-idler pairs, which will be modeled with the full joint Gaussian state description of its output. Propagation losses between the PBS and the atomic ensembles (labelled 'pre'), and between the atomic ensembles and the 50-50 beam splitter (labelled 'post') are modeled by fictitious beam splitters whose vacuum-state input ports inject Gaussian quantum noise. Finite quantum efficiency photodetectors (labelled 'pho') are similarly modeled, and we have ignored dark counts, which are known to be reasonably low at heralding wavelengths for silicon Geiger-mode avalanche photodiodes (APDs) [TYD+10]. Our number state model for these fictitious beam splitters, described in Section 3.2, includes the effects of phase differences between input ports, which we can use to characterize the effects of phase mismatch between pairs of ensembles. We will assume that any accumulated phase offsets leading to the ensembles can be incorporated into the pre-transmission efficiency.

The preceding imperfections expose two fundamentally different failure modes for this

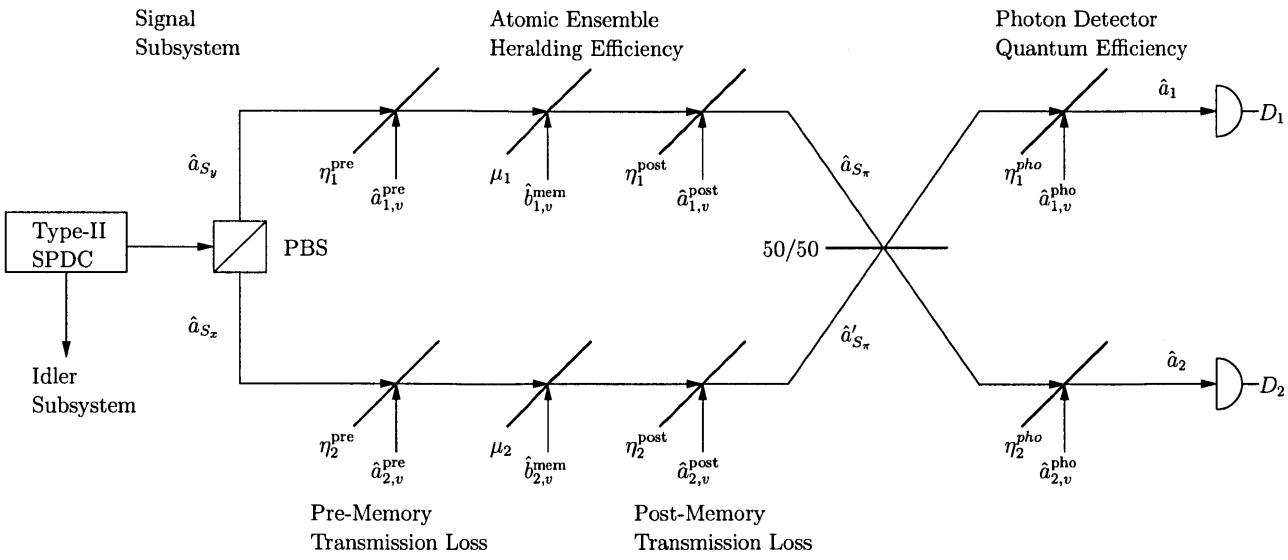

Figure 3-2: Hong-Ou-Mandel (HOM) interferometer measurement with loss (labeled).

protocol that affect fidelity and probability of success, respectively. First, is it possible for heralding detections at the APDs to declare the protocol's success even when the ensembles themselves are not in a polarization singlet state. For example, a multiple-pair event from the entanglement source could lead to multiple heralding photons emitted by a quantum memory. Post-memory attenuation and finite-quantum efficiency photodetection could eliminate all but one of those heralding photons, and the usage of Geiger-mode APDs might completely preclude our ability to distinguish between multiple-photon and single-photon events. A relative phase offset between two ensembles, either because of pump photon phase mismatch or pre-transmission phase accumulation, would similarly affect the final fidelity of the loaded quantum state. Lastly, because post-memory imperfections reduce potential heralding detections, it possible to declare the protocol a failure—and reduce the probability of success—even when the ensembles are successfully loaded.

3.2 Number State Fidelity and Success

We characterize this architecture's performance of heralding entanglement distribution by determining its fidelity figure-of-merit and measurement statistics under different photodetection schemes: photon-number resolving detection (PNRD), which can distinguish between

single-photon and multi-photon photodetection events; and non-resolving single-photon detection (NRPD), which is unable to exclude multi-photon error events. For these two schemes, the projective measurement operators $\hat{M}_j$ $(j = 1, 2, 3, 4)$ represent four successful heralding outcomes at the photodetectors D_i $(i = 1, 2, 3, 4)$. The input to each 50-50 beam splitter in Fig. 3-1 is a superposition state of linearly co-polarized heralding photons from the atomic memories, so we expect that successful entanglement distribution to yield single clicks at the signal and idler photodetector pairs. This DLCZ-like protocol for heralded polarization entanglement distribution therefore requires the occurrence of a single detection on either photodetectors D_1 or D_2, as well as a *corresponding event* on either D_4 or D_3. In the following, successful heralding is given by the projective measurements

$$\hat{M}_j^{\text{PNRD}} = \begin{cases} (|1\rangle_{11}\langle 1|) \otimes (|0\rangle_{22}\langle 0|) \otimes (|1\rangle_{33}\langle 1|) \otimes (|0\rangle_{44}\langle 0|) & j = 1 \\ (|0\rangle_{11}\langle 0|) \otimes (|1\rangle_{22}\langle 1|) \otimes (|1\rangle_{33}\langle 1|) \otimes (|0\rangle_{44}\langle 0|) & j = 2 \\ (|0\rangle_{11}\langle 0|) \otimes (|1\rangle_{22}\langle 1|) \otimes (|0\rangle_{33}\langle 0|) \otimes (|1\rangle_{44}\langle 1|) & j = 3 \\ (|1\rangle_{11}\langle 1|) \otimes (|0\rangle_{22}\langle 0|) \otimes (|0\rangle_{33}\langle 0|) \otimes (|1\rangle_{44}\langle 1|) & j = 4 \end{cases}, \tag{3.1}$$

$$\hat{M}_j^{\text{NRPD}} = \begin{cases} \left(\hat{I}_1 - |0\rangle_{11}\langle 0|\right) \otimes (|0\rangle_{22}\langle 0|) \otimes \left(\hat{I}_3 - |0\rangle_{33}\langle 0|\right) \otimes (|0\rangle_{44}\langle 0|) & j = 1 \\ (|0\rangle_{11}\langle 0|) \otimes \left(\hat{I}_2 - |0\rangle_{22}\langle 0|\right) \otimes \left(\hat{I}_3 - |0\rangle_{33}\langle 0|\right) \otimes (|0\rangle_{44}\langle 0|) & j = 2 \\ (|0\rangle_{11}\langle 0|) \otimes \left(\hat{I}_2 - |0\rangle_{22}\langle 0|\right) \otimes (|0\rangle_{33}\langle 0|) \otimes \left(\hat{I}_4 - |0\rangle_{44}\langle 0|\right) & j = 3 \\ \left(\hat{I}_1 - |0\rangle_{11}\langle 0|\right) \otimes (|0\rangle_{22}\langle 0|) \otimes (|0\rangle_{33}\langle 0|) \otimes \left(\hat{I}_4 - |0\rangle_{44}\langle 0|\right) & j = 4 \end{cases}, \tag{3.2}$$

where $|n\rangle_i$ $(n = 0, 1)$ are the vacuum and single-photon states, and $\hat{I}_i$ is the identity operator for the $\hat{a}_i$ mode measured at photodetector D_i $(i = 1, 2, 3, 4)$.

The heralding probability P_{herald} is the probability a heralding—a (D_1, D_2) single slick and a (D_3, D_4) single click. The success probability P_{success} is the probability that heralding has occurred and the four ensembles have loaded a polarization Bell state. The fidelity F_j is the projection of the post-heralding ensemble state onto the appropriate Bell state for $\hat{M}_j$

heralding, i.e.,

$$|\psi_j\rangle = \frac{1}{\sqrt{2}}\left(|1\rangle_S^1|0\rangle_S^2|0\rangle_S^3|1\rangle_S^4 + (-1)^j|0\rangle_S^1|1\rangle_S^2|1\rangle_S^3|0\rangle_S^4\right) \qquad (j=1,2,3,4)\,. \tag{3.3}$$

Following a photodetection measurement, the joint density operator of the four atomic ensembles is determined by applying $\hat{M}_j$ and tracing over the optical modes:

$$\hat{\rho}_{\text{post}}^j = \frac{1}{P_j^{\text{herald}}}\text{tr}_{1,2,3,4}\left(\hat{\rho}_{\text{out}}\hat{M}_j\right) \tag{3.4}$$

where $\hat{\rho}_{\text{out}}$ is the joint density operator of the heralding light fields and the ensembles

$$P_j^{\text{herald}} = \text{tr}\left(\hat{\rho}_{\text{out}}\hat{M}_j\right). \tag{3.5}$$

If $|\psi_j\rangle$ is the entangled state of the four ensembles as heralded by $\hat{M}_j$, and the entanglement storage fidelity is F_j, we find that the success probability is

$$P_{\text{success}} = \sum_{j=1}^{4} P_j^{\text{herald}} F_j = \sum_{j=1}^{4} \text{tr}\left(\hat{\rho}_{\text{out}}\hat{M}_j\right)\langle\psi_j|\,\hat{\rho}_{\text{post}}^j\,|\psi_j\rangle\,. \tag{3.6}$$

We will determine these measurement statistics using a full number-state analysis. Because the successful heralding outcomes defined by $\hat{M}_j$ are symmetric, all the fidelities F_j are equal to each other. We will, therefore, calculate only F_1 without any loss of generality. In what immediately follows, we will formalize our approach for calculating the joint density operator of the light-ensemble system following entanglement distribution.

3.2.1 Photon Number Probability Distributions

Our first task is to concisely represent the effects of propagation loss on light beams of arbitrary statistical composition, as shown by the unitary beam splitter transformation in Fig. 3-3. The matrix representation of linear-loss beam splitters in Fig. 3-2 corresponds to the SU (2) Lie group representation from angular momentum quantization [CST89]. We can use this equivalence to concisely relate the input and output field density operators from the loss using a joint photon-number probability distribution.

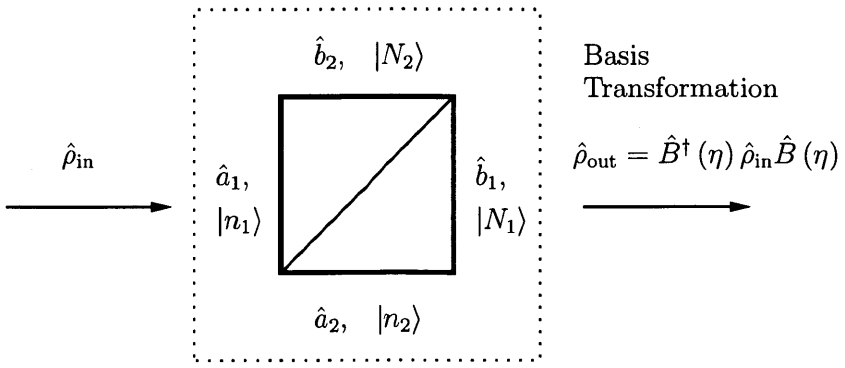

Figure 3-3: Beam splitter action on an input density operator $\hat{\rho}_{\text{in}}$ with two input ports and two output ports. Labeled at each port are the input and output bases used in Eqns. 3.10 and 3.11. The boson annihilation operations at the input and output are $\hat{a}_i$ and $\hat{b}_i$, respectively, and the accompanying index i represents signal ($i = 1$) and auxiliary modes ($i = 2$).

A two-port beam splitter with quantum efficiency η and input-field phase shifts ϕ_t and ϕ_r is described by the general SU (2) beam splitter operator,

$$\hat{B}(\eta, \phi_t, \phi_r) = e^{-i(\phi_t - \phi_r)\hat{L}_3} e^{-2i\cos^{-1}\left(\sqrt{\eta}\right)\hat{L}_2} e^{-i(\phi_t + \phi_r)\hat{L}_3}, \tag{3.7}$$

where the $\{\hat{L}_i\}$ are the Schwinger angular momentum operators for a two-dimensional quantum harmonic oscillator:

$$\hat{L}_1 = \frac{1}{2}\left(\hat{a}_1^{\dagger}\hat{a}_2 + \hat{a}_2^{\dagger}\hat{a}_1\right) \quad \hat{L}_2 = \frac{1}{2i}\left(\hat{a}_1^{\dagger}\hat{a}_2 - \hat{a}_2^{\dagger}\hat{a}_1\right) \quad \hat{L}_3 = \frac{1}{2}\left(\hat{a}_1^{\dagger}\hat{a}_1 + \hat{a}_2^{\dagger}\hat{a}_2\right). \tag{3.8}$$

Given a joint input state—either a pure state $|\psi\rangle_{\text{in}}$, or a pure or mixed state $\hat{\rho}_{\text{in}}$—of the signal and auxiliary inputs, the output state of the beam splitter is

$$|\psi_{\text{out}}\rangle = \hat{B}^{\dagger}(\eta, \phi_t, \phi_r)\,|\psi_{\text{in}}\rangle, \qquad \hat{\rho}_{\text{out}} = \hat{B}^{\dagger}(\eta, \phi_t, \phi_r)\,\hat{\rho}_{\text{in}}\hat{B}(\eta, \phi_t, \phi_r). \tag{3.9}$$

In the number-state representation, as shown in Fig. 3-3, the beam splitter output of a general joint input state

$$\hat{\rho}_{\text{in}} = \sum_{n_1, n_2 = 0}^{\infty} \sum_{n_1', n_2' = 0}^{\infty} \rho_{\text{in}}(n_1, n_2; n_1', n_2')\,|n_1, n_2\rangle\,\langle n_1', n_2'| \tag{3.10}$$

is,

$$\hat{\rho}_{\text{out}} = \sum_{N_1,N_2=0}^{\infty} \sum_{N_1',N_2'=0}^{\infty} \rho_{\text{out}}\left(N_1, N_2; N_1', N_2'\right) \left|N_1, N_2\right\rangle \left\langle N_1', N_2'\right|, . \tag{3.11}$$

The output state (Eqn. 3.11) follows from the input state (Eqn. 3.10) by first applying the unitary beam splitter transformation in Eqn. 3.7, and then inserting the identity operator in the $|N_1, N_2\rangle$ basis. The output matrix elements in Eqn. 3.11 are

$$\rho_{\text{out}}\left(N_1, N_2; N_1', N_2'\right) = \sum_{n_1,n_2=0} \sum_{n_1',n_2'=0} B_{N_1,N_2}^{n_1,n_2}\left(\eta, \phi_t, \phi_r\right) \left[B_{N_1',N_2'}^{n_1',n_2'}\left(\eta, \phi_t, \phi_r\right)\right]^* \rho_{\text{in}}\left(n_1, n_2; n_1', n_2'\right), \tag{3.12}$$

where

$$\begin{aligned} B_{N_1,N_2}^{n_1,n_2}\left(\eta, \phi_t, \phi_r\right) &= \left\langle N_1, N_2\right| \hat{B}^{\dagger}\left(\eta, \phi_t, \phi_r\right) \left|n_1, n_2\right\rangle \\ &= R_{N_1,N_2}^{n_1,n_2}\left(\eta\right) e^{i\phi_t(N_1-n_2)+\phi_r(N_1-n_1)}. \end{aligned} \tag{3.13}$$

The transformation coefficients,

$$R_{N_1,N_2}^{n_1,n_2}\left(\eta\right) = \left|B_{N_1,N_2}^{n_1,n_2}\left(\eta, \phi_t, \phi_r\right)\right| = \left\langle N_1, N_2\right| e^{-2i\cos^{-1}\left(\sqrt{\eta}\right)\hat{L}_2} \left|n_1, n_2\right\rangle, \tag{3.14}$$

can be calculated in terms of the Jacobi polynomials $P_n^{(\alpha,\beta)}\left(x\right)$ as

$$R_{N_1,N_2}^{n_1,n_2}\left(\eta\right) = \sqrt{\frac{N_1!N_2!}{n_1!n_2!}} \eta^{N_1-n_2}\left(1-\eta\right)^{N_1-n_1} P_{N_2}^{(N_1-n_1,N_1-n_2)}\left(2\eta-1\right), \qquad N_1 \geq n_1, n_2, \tag{3.15}$$

where

$$\begin{aligned} P_n^{(\alpha,\beta)}\left(x\right) = \frac{(-1)^n}{2^n n!}\left(1-x\right)^{-\alpha}\left(1+x\right)^{-\beta}\left(\frac{d}{dx}\right)^n \left[\left(1-x\right)^{n+\alpha}\left(1+x\right)^{n+\beta}\right], \\ \alpha, \beta > -1, \quad -1 \leq x \leq 1. \end{aligned} \tag{3.16}$$

The restriction $N_1 \geq n_1, n_2$ ensures the orthogonality of the Jacobi polynomials in Eqn. 3.15 over the range of quantum efficiency $0 \leq \eta \leq 1$; we will extend the range of this coefficient shortly. The R coefficient characterizes the output photon-number probability distribution for the joint input state $|n_1, n_2\rangle$. For a number-diagonal joint input state, it can be shown

that

$$P_{\text{out}}\left(N_1, N_2\right) = \left\langle N_1, N_2\right| \hat{\rho}_{\text{out}} \left|N_1, N_2\right\rangle = \sum_{\substack{n_1=0 \\ n_2=N_1+N_2-n_1}}^{N_1+N_2} P_{\text{out}}\left(N_1, N_2|n_1, n_2\right) P_{\text{in}}\left(n_1, n_2\right), \quad (3.17)$$

where the conditional and joint probabilities are

$$P_{\text{out}}\left(N_1, N_2|n_1, n_2\right) = \left[R^{n_1,n_2}_{N_1,N_2}\left(\eta\right)\right]^2 \quad \text{and} \quad P_{\text{in}}\left(n_1, n_2\right) = \rho_{\text{in}}\left(n_1, n_2; n_1, n_2\right), \quad (3.18)$$

respectively.

The beam splitter's physical symmetries allow us to extend the Jacobi polynomials over the full range photon-number output probabilities:

$$R^{n_1,n_2}_{N_1,N_2}\left(\eta\right) = \begin{cases} (-1)^{N_1-n_1} R^{N_1,N_2}_{n_1,n_2}\left(\eta\right) & n_2 \leq N_1 < n_1 \\ R^{N_2,N_1}_{n_2,n_1}\left(\eta\right) & n_1 \leq N_1 < n_2 \\ (-1)^{N_1-n_1} R^{n_2,n_1}_{N_2,N_1}\left(\eta\right) & n_1 > N_1,\ n_2 > N_1 \\ 0 & n_1 + n_2 \neq N_1 + N_2 \end{cases}. \quad (3.19)$$

We have made the unitary constraint explicit, as the Jacobi polynomials are not *ad hoc* restricted to events for which $n_1 + n_2 = N_1 + N_2$. Eqn. 3.12 simplifies because beam splitter unitarity requires $n_1 + n_2 = N_1 + N_2$ and $n'_1 + n'_2 = N'_1 + N'_2$. We thus eliminate the second and fourth summations in Eqn. 3.12 because $n_2 = N_1 + N_2 - n_1$ and $n'_2 = N'_1 + N'_2 - n'_1$, and restrict the remaining first and third summation there to $n_1 \in \{0, 1, \ldots, N_1 + N_2\}$ and $n'_1 \in \{0, 1, \ldots, N'_1 + N'_2\}$, respectively.

3.2.2 Calculation Examples

Accounting for each linear loss and interference element described in Figures 3-1 and 3-2, we calculate the singlet-distribution fidelity and the protocol's probability of success by applying compositions of the beam splitter transformation described in Eqn. 3.9 to the Gaussian input state whose low-flux approximations becomes the singlet state in Eqn. 1.5. Together, Eqns. 3.12 and 3.15 abstract the the beam splitter's action, in the number-state

basis, into a numerical calculation. Before analyzing the full architecture with all losses, we'll discuss two simpler calculations—lossless distribution and distribution with pre-transmission and photodetection losses—that form the repertoire of techniques necessary for analysis of the general problems of interest.

Lossless Case

Is the preceding mathematical formalism consistent with our expectations for lossless entanglement distribution? We assume that the input field phase shifts (ϕ_t, ϕ_r) are identically zero. Each of the four orthogonal signal and idler modes experience linear loss independently. Therefore, to avoid redundancy in the notation, we write the Gaussian state in Eqn. 1.5, at all orders, as

$$|\psi\rangle_{\text{in}} = \sum_{n,m=0}^{\infty} (-1)^n \sqrt{\frac{\bar{N}^{n+m}}{(1+\bar{N})^{n+m+2}}} |n\rangle_{S_y} |m\rangle_{S_x} |m\rangle_{I_y} |n\rangle_{I_x} \rightarrow \sum_{n,m=0}^{\infty} f_{n,m}(\bar{N}) |n_i\rangle^i , \quad (3.20)$$

where $f_{n,m}(\bar{N})$ abstracts the thermal statistics of the OPAs. Any state or term having a variable indexed by i $(i = 1, 2, 3, 4)$ actually denotes a product of four terms acting at separately on those photodetection branches, similar to Einstein index notation, so that $|n_i\rangle^i \equiv |n\rangle_{S_y} |m\rangle_{S_x} |m\rangle_{I_y} |n\rangle_{I_x}$ and any usage of the n_i will have a implicit dependence on n and m. The complete conversion of a pump field by a quantum memory is then given by $|N_i^a\rangle_a^i |0\rangle_b^i |0\rangle_S^i \rightarrow |0\rangle_a^i |N_i^a\rangle_b^i |N_i^a\rangle_S^i$, where a, b, and S denote the pump, heralding, and spin excitation modes, respectively. All photons impinging on the ensembles that form the memory are converted into heralding photons and spin excitations. The resulting state of the heralding photons and the spin excitations in therefore

$$\begin{aligned} |\psi\rangle_{\text{post-ensemble}} &= \sum_{n,m} (-1)^n \sqrt{\frac{\bar{N}^{n+m}}{(1+\bar{N})^{n+m+2}}} |n\rangle_b^1 |m\rangle_b^2 |m\rangle_b^3 |n\rangle_b^4 |n\rangle_S^1 |m\rangle_S^2 |m\rangle_S^3 |n\rangle_S^4 \\ &\rightarrow \sum_{n,m} f_{n,m}(\bar{N}) |n_i\rangle_b^i |n_i\rangle_S^i . \end{aligned} \quad (3.21)$$

Following interference of the heralding photons at the beam splitters in Fig. 3-1, the joint state of the ensembles and the heralding photons at the photodetectors is

$$|\psi\rangle_{\text{out}} = \sum_{N_i^p} \sum_{n,m} \underbrace{f_{n,m}\left(\bar{N}\right)}_{\text{SPDC}} \underbrace{B^{n,m}_{N_2^p,N_1^p}\left(\frac{1}{2}\right) B^{m,n}_{N_4^p,N_3^p}\left(\frac{1}{2}\right)}_{\text{Interference Amplitude}} |N_i^p\rangle_p^i \, |n_i\rangle_S^i \,, \tag{3.22}$$

where we have suppressed the phase arguments in the beam splitter coefficients because $\phi_t = \phi_r = 0$. In Eqn. 3.22, the interference amplitude terms correspond to the mixing of m and n photons at both the signal and idler subsystems in Fig. 3-1, yielding N_i^p photons photons at the photodetector D_i. The joint output written as a pure-state density operator is thus

$$\begin{aligned}\hat{\rho}_{\text{out}} = |\psi\rangle_{\text{out}} \langle\psi|_{\text{out}} = \sum_{N_i^p, N_i^{p'}} \sum_{n,m,n',m'} & f_{n,m}\left(\bar{N}\right) f_{n',m'}\left(\bar{N}\right) B^{n,m}_{N_2^p,N_1^p}\left(\frac{1}{2}\right) B^{m,n}_{N_4^p,N_3^p}\left(\frac{1}{2}\right) \\ & \cdot \left[B^{n',m'}_{N_2^{p'},N_1^{p'}}\left(\frac{1}{2}\right) B^{m',n'}_{N_4^{p'},N_3^{p'}}\left(\frac{1}{2}\right)\right]^* |N_i^p\rangle_p^i \, |n_i\rangle_S^i \, \langle N_i^{p'}|_{p'}^i \, \langle n_i'|_S^i \,.\end{aligned} \tag{3.23}$$

Following the definition of heralding probability in Eqn. 3.5, we trace over all modes and find that photon number resolving detectors yield

$$P_1^{\text{herald}} = \text{tr}\left(\hat{\rho}_{\text{out}} \hat{M}_1\right) = \sum_{n,m} \left| f_{n,m}\left(\bar{N}\right) B^{n,m}_{0,1}\left(\frac{1}{2}\right) B^{m,n}_{1,0}\left(\frac{1}{2}\right)\right|^2 = \frac{\bar{N}}{2\left(1+\bar{N}\right)^3}, \tag{3.24}$$

where the last equality is calculated by summation expansion. Following projective measurement, the joint state of the ensembles is given by the mixed-state density operator,

$$\begin{aligned}\hat{\rho}^1_{\text{post}} = \frac{1}{P_1^{\text{herald}}} \sum_{n,m,n',m'} & f_{n,m}\left(\bar{N}\right) f_{n',m'}\left(\bar{N}\right) B^{n,m}_{0,1}\left(\frac{1}{2}\right) B^{m,n}_{1,0}\left(\frac{1}{2}\right) \\ & \cdot \left[B^{n',m'}_{0,1}\left(\frac{1}{2}\right) B^{m',n'}_{1,0}\left(\frac{1}{2}\right)\right]^* |n_i\rangle_S^i \, \langle n_i'|_S^i \,,\end{aligned} \tag{3.25}$$

which, projected against the ideal singlet state $|\psi_1\rangle$ gives the fidelity of the entanglement distribution

$$\begin{aligned} F_1 &= \langle\psi_1|\,\hat{\rho}^1_{\text{post}}\,|\psi_1\rangle \\ &= \frac{1}{2P_1^{\text{herald}}} \sum_{n,m,n',m'} f_{n,m}\left(\bar{N}\right) f_{n',m'}\left(\bar{N}\right) B^{n,m}_{0,1}\left(\frac{1}{2}\right) B^{m,n}_{1,0}\left(\frac{1}{2}\right) \\ &\qquad \cdot \left[B^{n',m'}_{0,1}\left(\frac{1}{2}\right) B^{m',n'}_{1,0}\left(\frac{1}{2}\right)\right]^* \left(\delta_{n,1}\delta_{m,0} - \delta_{n,0}\delta_{m,1}\right)\left(\delta_{n',1}\delta_{m',0} - \delta_{n',0}\delta_{m',1}\right) \\ &= \frac{\bar{N}}{2P_1^{\text{herald}}\left(1+\bar{N}\right)^3} = 1, \end{aligned} \tag{3.26}$$

Here, the second and third terms from expanding the Kronecker delta expression cancel, and the last equality follows from Eqn. 3.24. Unity fidelity is the expected result in this ideal, lossless case. Because the post-measurement state is symmetric with respect to all $\hat{M}_j$, the protocol's overall success probability—defined by Eqn. 3.6—is four times the value we found in Eqn. 3.24,

$$P_{\text{success}} = \frac{2\bar{N}}{\left(1+\bar{N}\right)^3}, \tag{3.27}$$

which equals the probability of successful generation of a single pair of signal and idler photons from a dual OPA source. Again, this is an expected result for the ideal case of lossless operation.

The non-resolving photodetection calculations are a bit more complicated, and there we use the identity

$$\text{tr}\left[|n\rangle\langle n'|\left(I - |0\rangle\langle 0|\right)\right] = 1 - \delta_{n,0}\delta_{n',0} \tag{3.28}$$

and the prior definition of a NRPD POVM measurement given in Eqn. 3.2. Applied to the joint state density operator in Eqn. 3.23, the post-measurement state of the ensembles is

$$\begin{aligned} \hat{\rho}^1_{\text{post}} &= \sum_{N_i^p, N_i^{p'}} \sum_{n,m,n',m'} f_{n,m}\left(\bar{N}\right) f_{n',m'}\left(\bar{N}\right) B^{n,m}_{0,N_1^p}\left(\frac{1}{2}\right) B^{m,n}_{N_4^p,0}\left(\frac{1}{2}\right)\left[B^{n',m'}_{0,N_1^{p'}}\left(\frac{1}{2}\right) B^{m',n'}_{N_4^{p'},0}\left(\frac{1}{2}\right)\right]^* \\ &\qquad \cdot \left(1 - \delta_{0,N_1^p}\delta_{0,N_1^{p'}} - \delta_{0,N_4^p}\delta_{0,N_4^{p'}} + \delta_{0,N_1^p}\delta_{0,N_1^{p'}}\delta_{0,N_4^p}\delta_{0,N_4^{p'}}\right)|n_i\rangle^i_S\,\langle n'_i|^i_S \\ &= \sum_{n,m}\left|f_{n,m(\bar{N})} B^{n,m}_{0,n+m}\left(\frac{1}{2}\right) B^{m,n}_{n+m,0}\left(\frac{1}{2}\right)\right|^2 |n_i\rangle^i_S\,\langle n_i|^i_S \end{aligned} \tag{3.29}$$

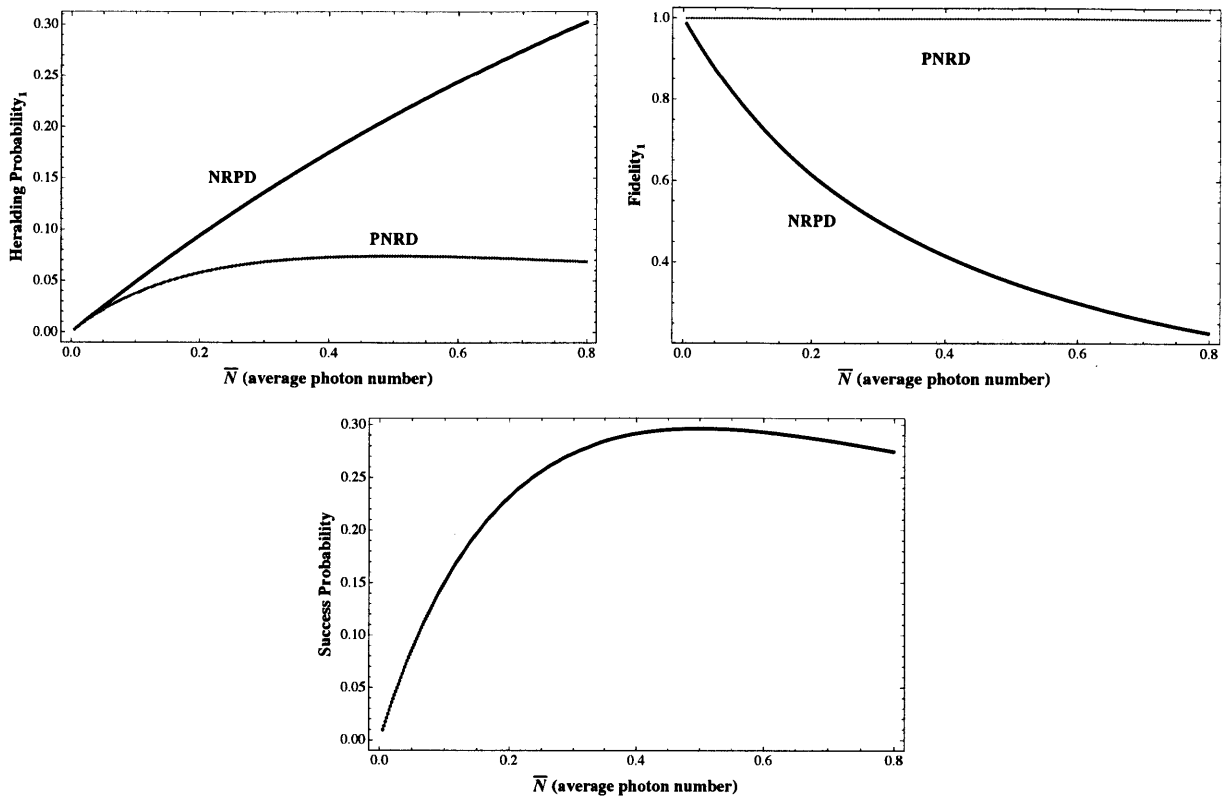

Figure 3-4: Figures of merit for lossless architecture (PNRD and NRPD). Figures 3-4(a) and 3-4(b) show divergences between heralding probability and fidelity for PNRD (gray) and NRPD (black) architectures. The protocol's overall success probability is identical in either case (Fig. 3-4(c)).

In the last step's simplification, we have enforced the photon number conservation constraint implicit in the definition of the beam splitter coefficient. For the sake of brevity, the details of the corresponding fidelity, heralding probability, and success probability calculations are omitted, being straightforward extensions of PNRD calculation. Fig. 3-4 shows the combined results of the PNRD and NRPD calculations.

Despite the absence of losses in this example, we can still gain some intuition for the effects of different photodetection schemes on our figures of merit. Fig. 3-4 compares the resulting figures of merit between the PNRD and NRPD photodetection schemes in a lossless architecture in which increasing $\bar{N}$ leads to an increasing likelihood of multi-pair emissions from the entanglement source. The heralding probability for the NRPD exceeds that for PNRD, which is not surprising, as PNRD forms a subset of the possible detection events present with the NRPD scheme. In the absence of loss, the NRPD fidelity is independent

of detection events at either D_1/D_4 or D_2/D_3 and falls dramatically for high values of $\bar{N}$, being ultimately unable to distinguish between valid single-photon heralding events and higher-order excitations stored in the ensemble. The PNRD fidelity, on the other hand, holds at unity, because this detector perfectly identifies single-pair loading in the lossless scenario under consideration here. The success probability, however, is identical for the PNRD and NRPD schemes, because any decline in NRPD fidelity is compensated for by a corresponding increase in heralding probability. A single term in the success probability sum—the product of the fidelity and heralding probability—represents the joint probability of loading the required Bell state and the measurement of the corresponding heralding event. Single photon events do not require photon-number resolving capabilities, and as such, the loading success is equally likely under either scheme, when the system is lossless.

Pre-Transmission and Photodetection Losses

Including loss in our analysis introduces nested binomial distributions of pump and signal photons, and the added computational complexity of deeper and deeper nested summations. As such, the results of this example and all subsequent sections are calculated numerically, with a range of $\bar{N}$ chosen so that the input Gaussian state can be safely truncated to a finite number of excitations. For all subsequent calculations in this thesis, $\bar{N}$ ranges from 0.05 to 0.3 in steps of $\Delta\bar{N} = 0.05$, and we take $n_{\max} = m_{\max} = 3$ to be the maximum number of excitations. For the the full range of a single transmission efficiency $0 \leq \eta \leq 1$, it can be shown (numerically) that figures of merit, such as heralding probability, with higher truncation values differ insignificantly from those calculated at $n_{\max} = m_{\max} = 3$.

Introducing auxiliary vacuum states indexed by N^{pre} and N^{pho}, the joint output state of the heralded photons, ensemble excitations, and noise modes is given by,

$$|\psi\rangle_{\text{out}} = \sum_{N_i^a, N_i^{\text{pre}}, N_i, N_i^{\text{pho}}} \sum_{n,m} f_{n,m}\left(\bar{N}\right) B^{n_i,0}_{N_i^a,N_i^{\text{pre}}}\left(\eta_i^{\text{pre}}\right) B^{N_1^a,N_2^a}_{N_2,N_1}\left(\frac{1}{2}\right) B^{N_3^a,N_4^a}_{N_4,N_3}\left(\frac{1}{2}\right) \cdot B^{N_i,0}_{N_i^p,N_i^{\text{pho}}}\left(\eta_i^{\text{pho}}\right) |N_i^p\rangle_p^i \, |N_i^a\rangle_S^i \, |N_i^{\text{pre}}\rangle_{\text{pre}}^i \left|N_i^{\text{pho}}\right\rangle_{\text{pho}}^i . \quad (3.30)$$

Eqn. 3.30 contains several important features. First, recall that each term indexed by i

actually represents four independent terms. The n_i photons from the SPDC source mix with vacuum (zero photons), converting into N_i^a pump photons for the quantum memory and N_i^{pre} noise photons. The pump photons are completely converted into N_i^a heralding photons and N_i^a spin excitations. At the 50-50 beam splitter, the (N_1^a, N_2^a) and (N_3^a, N_4^a) photons interfere, yielding (N_1, N_2) and (N_3, N_4) photons which are each mixed with vacuum to yield N_i^p photons at each D_i photodetector. The summation lower limit for each summation variable is 0, and upper limit is given by the sum of the inputs to a given beam splitter (e.g., n_i for each the N_i^a and N_i^{pre} summations, $N_1^a + N_2^a$ for each of the N_1 and N_2 summations). Tracing out the noise modes and and applying photon-number conservation to eliminate nested summations, the PNRD heralding probability for single-photon counts at detectors D_1 and D_4 is given by

$$P_1^{\text{PNRD}} = \sum_{N_i^a, N_i} \sum_{n,m} \left| f_{n,m}\left(\bar{N}\right) B^{n_i,0}_{N_i^a, n_i - N_i^a}\left(\eta_i^{\text{pre}}\right) B^{N_1^a, N_2^a}_{N_2, N_1}\left(\frac{1}{2}\right) B^{N_3^a, N_4^a}_{N_4, N_3}\left(\frac{1}{2}\right) \right.$$
$$\left. \cdot\, B^{N_1,0}_{1, N_1 - 1}\left(\eta_1^{\text{pho}}\right) B^{N_2,0}_{0, N_2}\left(\eta_2^{\text{pho}}\right) B^{N_3,0}_{0, N_3}\left(\eta_3^{\text{pho}}\right) B^{N_4,0}_{1, N_4 - 1}\left(\eta_4^{\text{pho}}\right) \right|^2 . \quad (3.31)$$

From Eqn. 3.15, the photon-number probability amplitude following the OPA coefficient corresponds to the familiar binomial probability distribution that results from mixing of a number state with vacuum. Applying the NRPD POVM and photon-number conservation, as in Eqn. 3.25, and factoring the remaining photodetection efficiency amplitudes gives the heralding probability:

$$P_1^{\text{NRPD}} =$$
$$\sum_{N_i^a, N_i} \sum_{n,m} \left| f_{n,m}\left(\bar{N}\right) B^{n_i,0}_{N_i^a, n_i - N_i^a}\left(\eta_i^{\text{pre}}\right) B^{N_1^a, N_2^a}_{N_2, N_1}\left(\frac{1}{2}\right) B^{N_3^a, N_4^a}_{N_4, N_3}\left(\frac{1}{2}\right) B^{N_2,0}_{0, N_2}\left(\eta_2^{\text{pho}}\right) B^{N_3,0}_{0, N_3}\left(\eta_3^{\text{pho}}\right) \right|^2$$
$$\left[\left| B^{N_1,0}_{0, N_1}\left(\eta_1^{\text{pho}}\right) \right|^2 - \sum_{N_1^p = 0}^{N_1} \left| B^{N_1,0}_{N_1^p, N_1 - N_1^p}\left(\eta_1^{\text{pho}}\right) \right|^2 \right] \left[\left| B^{N_4,0}_{0, N_4}\left(\eta_4^{\text{pho}}\right) \right|^2 - \sum_{N_4^p = 0}^{N_4} \left| B^{N_4,0}_{N_4^p, N_4 - N_4^p}\left(\eta_4^{\text{pho}}\right) \right|^2 \right] . \quad (3.32)$$

The terms of this summation are also the diagonal coefficients of the ensembles' post-measurement density operator, which is required for calculating the fidelity and overall

success probability of the protocol. To avoid redundancy, the numerical calculations of these quantities and their interpretation is described in Section 3.2.3.

3.2.3 Full Loss Calculation (PNRD and NRPD)

In the previous section, we previewed a set of techniques used in the analysis of entanglement distribution, which we now use to account for all losses. In the following, we assume that the input field phase shifts (ϕ_t, ϕ_r) of each loss-modeling beam splitter are identically 0. As in the previous sections, we only list expressions for matching photodetection events at D_1 and D_4, as corresponding expressions for D_2 and D_3 are found by simple substitution. Accounting for all losses, the full output state of the architecture, as shown in Fig. 3-2, is given by,

$$
\begin{aligned}
|\psi\rangle_{\text{out}} = & \sum_{n,m} f_{n,m}\left(\bar{N}\right) \\
& \cdot \sum_{\substack{N_i^a, N_i^{\text{pre}}, N_i^l, N_i^{\text{post}}, \\ N_i, N_i^p, N_i^{\text{pho}}}} \Bigg[\underbrace{B^{n_i,0}_{N_i^a,N_i^{\text{pre}}}\left(\eta_i^{\text{pre}}\right) B^{N_i^a,0}_{N_i^l,N_i^{\text{post}}}\left(\eta_i^{\text{post}}\right)}_{\text{Pre-Interference Loss}} \underbrace{B^{N_1^l,N_2^l}_{N_2,N_1}\left(\frac{1}{2}\right) B^{N_3^l,N_4^l}_{N_4,N_3}\left(\frac{1}{2}\right)}_{\text{Interference Terms}} \underbrace{B^{N_i,0}_{N_i^p,N_i^{\text{pho}}}\left(\eta_i^{\text{pho}}\right)}_{\text{Photodetection Loss}} \Bigg] \\
& \cdot \underbrace{|N_i^p\rangle_p^i \, |N_i^a\rangle_S^i}_{\text{Heralded \& Ensemble Modes}} \underbrace{\left|N_i^{\text{pho}}\right\rangle_{\text{pho}}^i \left|N_i^{\text{post}}\right\rangle_{\text{post}}^i \left|N_i^{\text{pre}}\right\rangle_{\text{pre}}^i}_{\text{Auxiliary Noise Modes}} .
\end{aligned} \tag{3.33}
$$

and the corresponding joint density operator of the heralded photon and ensemble modes is

$$
\begin{aligned}
\hat{\rho}_{\text{out}}^{p,S} = & \sum_{n,m,n',m'} f_{n,m}\left(\bar{N}\right) f_{n',m'}\left(\bar{N}\right) \\
& \cdot \sum_{\substack{N_i^a, N_i^{\text{pre}} \\ N_i^{a\prime}}} \sum_{\substack{N_i^l, N_i^{\text{post}} \\ N_i^{l\prime}}} B^{n_i,0}_{N_i^a,N_i^{\text{pre}}}\left(\eta_i^{\text{pre}}\right) B^{N_i^a,0}_{N_i^l,N_i^{\text{post}}}\left(\eta_i^{\text{post}}\right) \left[B^{n_i',0}_{N_i^{a\prime},N_i^{\text{pre}}}\left(\eta_i^{\text{pre}}\right) B^{N_i^{a\prime},0}_{N_i^{l\prime},N_i^{\text{post}}}\left(\eta_i^{\text{post}}\right) \right]^* \\
& \cdot \sum_{\substack{N_1,N_2,N_3,N_4 \\ N_1',N_2',N_3',N_4'}} B^{N_1^l,N_2^l}_{N_2,N_1}\left(\frac{1}{2}\right) B^{N_3^l,N_4^l}_{N_4,N_3}\left(\frac{1}{2}\right) \left[B^{N_1^{l\prime},N_2^{l\prime}}_{N_2',N_1'}\left(\frac{1}{2}\right) B^{N_3^{l\prime},N_4^{l\prime}}_{N_4',N_3'}\left(\frac{1}{2}\right) \right]^* \\
& \cdot \sum_{\substack{N_i^p, N_i^{\text{pho}} \\ N_i^{p\prime}}} B^{N_i,0}_{N_i^p,N_i^{\text{pho}}}\left(\eta_i^{\text{pho}}\right) \left[B^{N_i',0}_{N_i^{p\prime},N_i^{\text{pho}}}\left(\eta_i^{\text{pho}}\right) \right]^* |N_i^p\rangle_p^i \, |N_i^a\rangle_S^i \, \langle N_i^{p\prime}|_p^i \, \langle N_i^{a\prime}|_S^i ,
\end{aligned} \tag{3.34}
$$

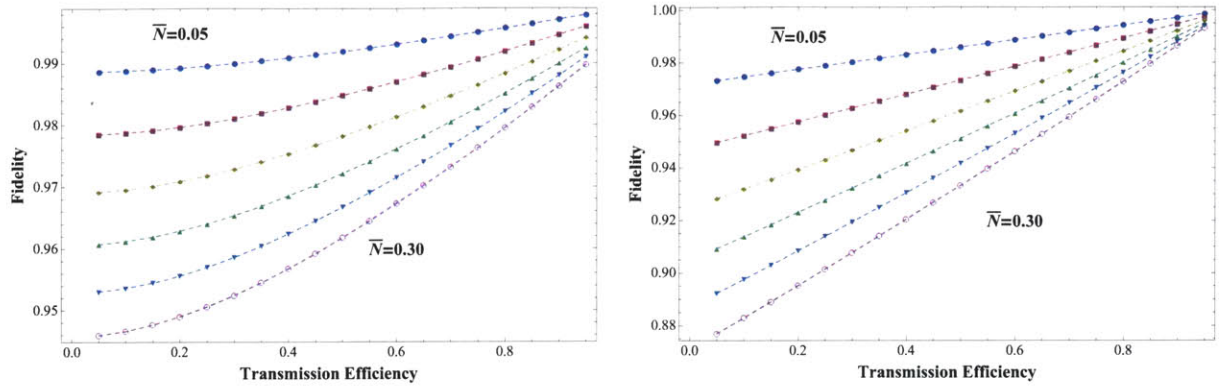

(a) Single loss (η_1^{pre}).

(b) Signal path losses (η_1^{pre} and η_2^{pre}).

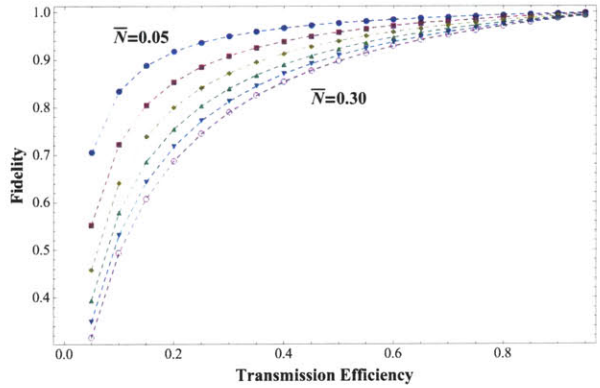

(c) Mis-matched losses (η_1^{pre} and η_3^{pre}).

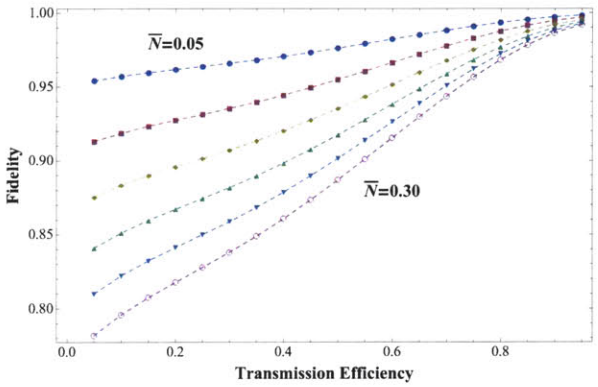

(d) Matched losses (η_1^{pre} and η_4^{pre}).

Figure 3-5: F_1 fidelities with non-uniform pre-transmission losses (PNRD) for $\bar{N} = 0.05 - 0.3$ $\left(\Delta\bar{N} = 0.05\right)$. The caption in each subfigure specifies which of η_i^{pre} $(i = 1, 2, 3, 4)$ is varied for that calculation; those not specified are fixed at 0.9.

and the PNRD probability that a heralding event $\hat{M}_1$ has occurred is then

$$\begin{aligned} P_1 &= \text{tr}\left(\hat{\rho}_{\text{out}}^{p,S} M_1\right) \\ &= \sum_{n,m}^{\infty} \left[f_{n,m}\left(\bar{N}\right)\right]^2 \sum_{N_i^a, N_i^l} \sum_{\substack{N_1,N_2,\\ N_3,N_4}} \left| B_{N_i^a, n_i - N_i^a}^{n_i,0}\left(\eta_i^{\text{pre}}\right) B_{N_i^l, N_i^a - N_i^l}^{N_i^a,0}\left(\eta_i^{\text{post}}\right) B_{N_2,N_1}^{N_1^l,N_2^l}\left(\frac{1}{2}\right) B_{N_4,N_3}^{N_3^l,N_4^l}\left(\frac{1}{2}\right) \right. \\ &\quad \left. \cdot B_{1,N_1-1}^{N_1,0}\left(\eta_1^{\text{pho}}\right) B_{0,N_2}^{N_2,0}\left(\eta_2^{\text{pho}}\right) B_{0,N_3}^{N_3,0}\left(\eta_3^{\text{pho}}\right) B_{1,N_4-1}^{N_4,0}\left(\eta_4^{\text{pho}}\right) \right|^2 . \end{aligned} \tag{3.35}$$

The results of numerical calculations with these expressions are shown in Figures 3-6 and 3-5. These figures distinguish between what we term 'uniform' and 'non-uniform' losses. Fig. 3-6 assumes that varying pre-transmission and photodetection losses are *identical* for all four arms of the interferometer, whereas Fig. 3-5 makes no such assumption by considering

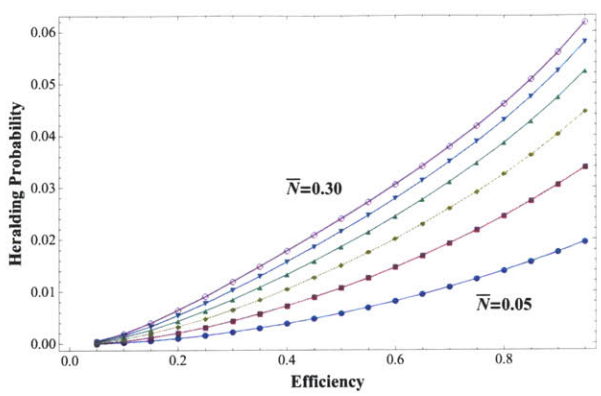

(a) Heralding probability (uniform loss).

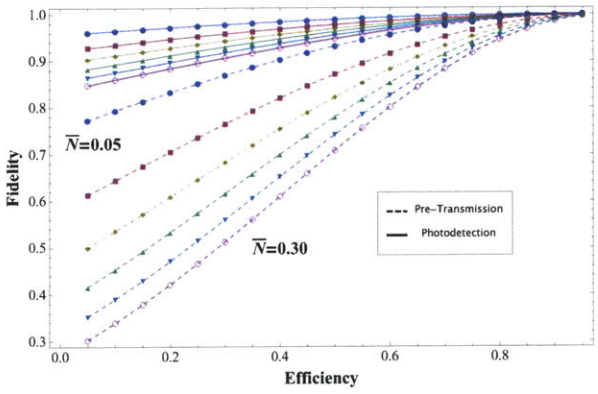

(b) Fidelity (pre- and photodetection losses).

Figure 3-6: Figures of merit with uniform losses (PNRD) for $\bar{N} = 0.05 - 0.3$ $\left(\Delta\bar{N} = 0.05\right)$. Heralding probabilities are independent of a uniform loss' location: either before (pre-transmission) or after (post-transmission or photodetection) the ensemble (Fig. 3-6(a)). Pre-transmission losses preferentially decrease the fidelity of entanglement distribution compared to post-transmission and photo-detection losses (Fig. 3-6(b)).

the effects of only a *single* loss or *paired* losses as labelled in the captions. The presence of uniform losses in one location—before or after the ensembles or during photodetections—has identical effects on the heralding probability. This heralding probability doesn't depend on where a single uniform loss is located, as a pump photon lost prior to the ensemble or a heralding photon lost after the ensemble ultimately will have the same heralding result. This is definitely not the case for the F_1 fidelity, as a pre-transmission loss of a pump photon precludes successful entanglement distribution. In this case, it is difficult to tell if matching signal and idler photons were stored simultaneously. By contrast, any post-transmission or photodetection loss has a much smaller effect on the fidelity. Post-transmission and photodetection loss are quantitatively equal in their fidelity effects. Lastly, increasing pump power in the OPA source matches intuition, as increasing $\bar{N}$ makes heralding events more likely, but decreases the desired fidelity due to multiple-pair effects.

In Fig. 3-5, we see that fidelity of entanglement is fairly robust against a single pre-transmission loss, as well as uniform losses present only in the signal subsystem or uniform losses between paths matched for a successful heralding event detection. Uniform losses shared between mis-matched paths (e.g., varying η_1 and η_3) degrade fidelity significantly, almost as though transmission loss were uniformly shared by all the paths as in Fig. 3-6(b).

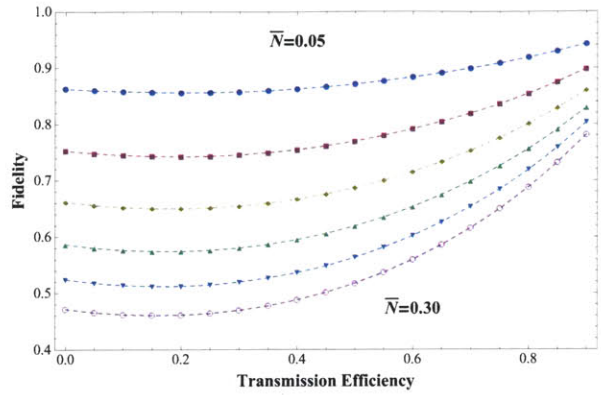

(a) F_1, uniform pre-transmission loss (η^{pre}).

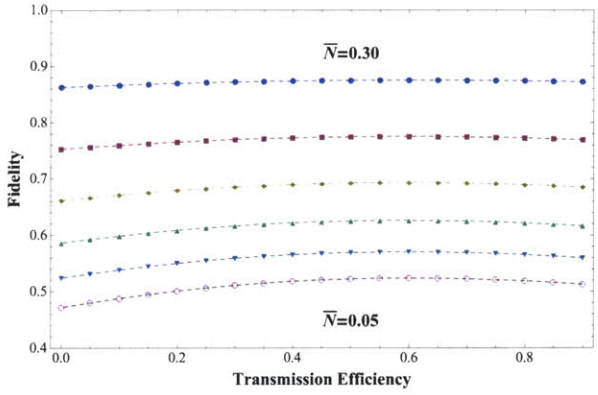

(b) F_1, uniform photodetection loss (η^{pho}).

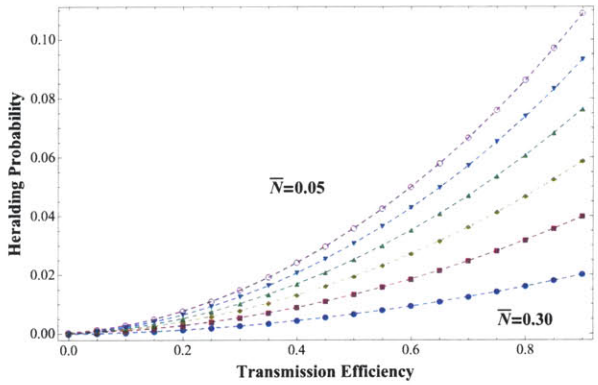

(c) Heralding probability (any uniform loss).

Figure 3-7: Figures of merit with uniform losses (NRPD) for $\bar{N} = 0.05 - 0.3$ ($\Delta N = 0.05$). Figures 3-7(a) and 3-7(b) show the F_1 fidelities for varying pre-transmission and photodetection efficiencies, respectively, with all other efficiencies fixed at $\eta = 0.9$. Fig. 3-7(c) shows heralding probability for varying pre-transmission efficiency.

The remaining analysis case is non-resolving photodetection (NRPD), which we show in Fig. 3-7. The details of this calculation are nearly identical to that shown in Sections 3.2.2 and 3.2.2. Not surprisingly, as in the lossless NRPD analysis, the heralding probability is higher than in the PNRD case, and increasing $\bar{N}$ severely diminishes fidelity when both pre-transmission and photodetection losses occur. In the case of the latter, photodetection loss has almost no effect on the final fidelity of entanglement distribution. Pre-transmission losses in Fig. 3-7(a) demonstrate a residual dependence on pre-transmission loss for higher transmission efficiencies, consistent with our prior PNRD analysis.

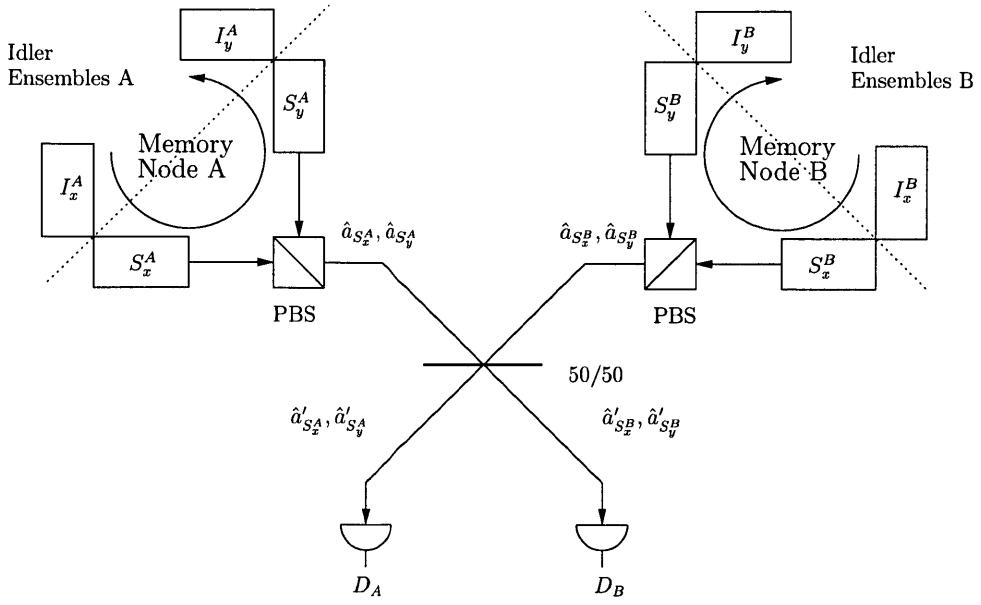

Figure 3-8: Polarization entanglement connection. We assume that ensembles A and B are independently in polarization singlet states or Gaussian states following entanglement distribution in Section 3.1. The anti-Stokes photons from reading the A and B signal ensembles are interfered at the 50-50 beam splitter. Photon detections at D_A *and* D_B heralds entanglement connection between the idler ensembles A and B.

3.3 Quantum Communication with Atomic Ensembles and Polarization Entanglement

After successfully distributing entanglement to a pair of nodes, resulting in local entanglement, we will want to extend our quantum communication capabilities over distances prohibited by direct transmission. In this section, we use post-selected, polarization-entangled ensembles to accomplish a basic task in long-distance quantum communication, namely entanglement swapping. The high level concepts underlying this procedure was described in Section 1.2.1 of this thesis' introduction, and is a modification of the DLCZ protocol's application to quantum communication [DLCZ01].

3.3.1 Entanglement Connection

Fig. 3-8 outlines a procedure for accomplishing polarization entanglement connection with atomic ensembles. Polarization entanglement is generated independently, at two different

nodes, as described in Section 3.1 and Fig. 1-3(a). A Bell-state measurement between the $\left(S_y^A, S_x^A\right)$ and $\left(S_y^B, S_x^B\right)$ ensemble pairs establishes polarization entanglement between the remaining idler ensemble pairs $\left(I_y^A, I_x^A\right)$ and $\left(I_y^B, I_x^B\right)$. Coherent, on-resonance pulses at each of the signal ensembles reads a Dicke excitation out of the $|s\rangle - |e\rangle$ atomic transition into a well-defined spatial mode. Loss-modeling beam splitters before interference (η_{pre}) and at photodetection (η_{pho}) characterize the quantum efficiency losses, although to maintain consistency with [RS06], we calculate fidelity with respect to $\eta_{\text{meas}} = \eta_{\text{pre}}\eta_{\text{pho}}$. In the following, we determine the fidelity and probability of success when ensembles A and B are independently in singlet or Gaussian states.

Although a full Bell state measurement is not possible using linear optics [LCS99], the observation of single clicks at both D_A and D_B, when these are unity quantum efficiency photon-number resolving detectors, uniquely heralds the measurement of a singlet state and successful completion of entanglement connection protocol when the A and B ensembles were both in their singlet states. Two signal ensemble pairs in independent singlet states can be separated into four orthogonal basis states

$$\begin{aligned} |\psi\rangle^A \otimes |\psi\rangle^B &= \frac{1}{\sqrt{2}}\left(|1\rangle_{S_y^A}|0\rangle_{S_x^A}|0\rangle_{I_y^A}|1\rangle_{I_x^A} - |0\rangle_{S_y^A}|1\rangle_{S_x^A}|1\rangle_{I_y^A}|0\rangle_{I_x^A}\right) \\ &\quad \otimes \frac{1}{\sqrt{2}}\left(|1\rangle_{S_y^B}|0\rangle_{S_x^B}|0\rangle_{I_y^B}|1\rangle_{I_x^B} - |0\rangle_{S_y^B}|1\rangle_{S_x^B}|1\rangle_{I_y^B}|0\rangle_{I_x^B}\right) \\ &= |\phi_{yy}\rangle + |\phi_{yx}\rangle + |\phi_{xy}\rangle + |\phi_{xx}\rangle\,, \end{aligned} \tag{3.36}$$

where each $|\phi_{ij}\rangle$ $(i,j = x,y)$ labels a joint state with signal-photon polarizations i and j in each path prior to interference. Because of photon-twinning at interference, only two of these orthogonal states—$|\phi_{xy}\rangle$ and $|\phi_{yx}\rangle$—contribute to the probability of a heralding event: either $(\hat{x},\hat{y})$- or $(\hat{y},\hat{x})$-polarized photon pairs at (D_A, D_B), with equal probability. As such, the entanglement connection fidelity will be unity in both the PNRD and the NPRD cases—

$$F_C = \frac{P_{\text{success}}}{P_{\text{herald}}} = \frac{P_{xy} + P_{yx}}{P_{xy} + P_{yx}} = 1 \tag{3.37}$$

—independent of pre-transmission and photodetection quantum efficiency losses.

Now let us consider performance when ensembles A and B are modeled as being in

Gaussian states parameterized by an average spin excitation number $\bar{N}$. In the absence of any important nonlinear elements in Fig. 3-8, we will perform a characteristic function analysis instead of a number-state analysis. The joint density operator of these ensembles is $\hat{\rho}_{SI}^{\text{in}} = \hat{\rho}_{SI}^{A} \otimes \hat{\rho}_{SI}^{B}$, where $\hat{\rho}_{SI}^{i} = \hat{\rho}_{S_x^i I_y^i} \otimes \hat{\rho}_{S_y^i I_x^i}$ $(i = A, B)$, which is represented by the anti-normally ordered characteristic function,

$$\begin{aligned}
\chi_A^{\rho_{\text{in}}}(\boldsymbol{\zeta}) &= \langle D_A\left(\hat{a}_{S_y^A}, \zeta_{S_y^A}\right) D_A\left(\hat{a}_{S_x^A}, \zeta_{S_x^A}\right) D_A\left(\hat{S}_{I_y^A}, \zeta_{I_y^A}\right) D_A\left(\hat{S}_{I_x^A}, \zeta_{I_x^A}\right) \\
&\quad \cdot D_A\left(\hat{a}_{S_y^B}, \zeta_{S_y^B}\right) D_A\left(\hat{a}_{S_x^B}, \zeta_{S_x^B}\right) D_A\left(\hat{S}_{I_y^B}, \zeta_{I_y^B}\right) D_A\left(\hat{S}_{I_x^B}, \zeta_{S_x^B}\right)\rangle \\
&= \exp\Big[-\left(1+\bar{N}\right)\left(|\zeta_{S_y^A}|^2 + |\zeta_{S_x^A}|^2 + |\zeta_{I_y^A}|^2 + |\zeta_{I_x^A}|^2\right) \\
&\quad - \left(1+\bar{N}\right)\left(|\zeta_{S_y^B}|^2 + |\zeta_{S_x^B}|^2 + |\zeta_{I_y^B}|^2 + |\zeta_{I_x^B}|^2\right) \\
&\quad + 2\text{Re}\left(\tilde{N}\zeta_{S_x^A}\zeta_{I_y^A}\right) - 2\text{Re}\left(\tilde{N}\zeta_{S_y^A}\zeta_{I_x^A}\right) \\
&\quad + 2\text{Re}\left(\tilde{N}\zeta_{S_x^B}\zeta_{I_y^B}\right) - 2\text{Re}\left(\tilde{N}\zeta_{S_y^B}\zeta_{I_x^B}\right)\Big],
\end{aligned} \tag{3.38}$$

where $\tilde{N} = \sqrt{\bar{N}\left(\bar{N}+1\right)}$, $D_A\left(\hat{a}_i, \zeta_i\right) = e^{-\zeta_i^* \hat{a}_i} e^{\zeta_i \hat{a}_i^\dagger}$ is the antinormally-ordered displacement operator, and

$$\boldsymbol{\zeta} = [\boldsymbol{\zeta}_S, \boldsymbol{\zeta}_I]^T = \left[\zeta_{S_y^A}, \zeta_{S_y^B}, \zeta_{S_x^A}, \zeta_{S_x^B}, \zeta_{I_y^A}, \zeta_{I_y^B}, \zeta_{I_x^A}, \zeta_{I_x^B}\right]^T. \tag{3.39}$$

The optical modes reaching the detectors D_i in Fig. 3-2 are

$$\hat{\mathbf{a}}_S^{\text{out}} = \sqrt{\eta^{\text{pho}}\eta^{\text{pre}}}\mathbf{B}\hat{\mathbf{a}}_{\text{in}}^{\text{S}} + \sqrt{\eta^{\text{pho}}\left(1-\eta^{\text{pre}}\right)}\mathbf{B}\hat{\mathbf{a}}_v^{\text{pre}} + \sqrt{1-\eta^{\text{pho}}}\hat{\mathbf{a}}_v^{\text{pho}} \tag{3.40}$$

where we have defined the operator-valued vectors

$$\begin{aligned}
\hat{\mathbf{a}}_S^{\text{out}} &= \left[\hat{a}'_{S_y^A}, \hat{a}'_{S_y^B}, \hat{a}'_{S_x^A}, \hat{a}'_{S_x^B}\right]^{\text{T}} \\
\hat{\mathbf{a}}_S^{\text{in}} &= \left[\hat{a}_{S_y^A}, \hat{a}_{S_y^B}, \hat{a}_{S_x^A}, \hat{a}_{S_x^B}\right]^{\text{T}} \\
\hat{\mathbf{a}}^{\text{pre}} &= [\hat{a}_1^{\text{pre}}, \ldots, \hat{a}_4^{\text{pre}}]^{\text{T}} \\
\hat{\mathbf{a}}^{\text{pho}} &= \left[\hat{a}_1^{\text{pho}}, \ldots, \hat{a}_4^{\text{pho}}\right]^{\text{T}}
\end{aligned} \tag{3.41}$$

with the linear transformation of the signal modes:

$$\mathbf{B} = \begin{bmatrix} \mathbf{M}_{2\times2} & \mathbf{0}_{2\times2} \\ \mathbf{0}_{2\times2} & \mathbf{M}_{2\times2} \end{bmatrix} \qquad \mathbf{M}_{2\times2} = \frac{1}{\sqrt{2}} \begin{bmatrix} 1 & 1 \\ 1 & -1 \end{bmatrix}. \tag{3.42}$$

All of the idler modes $\hat{\mathbf{S}}_I^{\text{in}} = \left[\hat{S}_{I_y^A}, \hat{S}_{I_y^B}, \hat{S}_{I_x^A}, \hat{S}_{I_x^B}\right]^{\text{T}}$ remain unchanged. The Gaussian mixed-state of the Stokes light arriving at the detectors and the idler ensemble excitations is given by the antinormally-ordered characteristic function

$$\begin{aligned} \chi_A^{\rho_{\text{out}}}\left(\boldsymbol{\zeta}, \tilde{\boldsymbol{\zeta}}\right) &= \langle D_A\left(\hat{\mathbf{a}}_S^{\text{out}}, \boldsymbol{\zeta}_S\right) D_A\left(\hat{\mathbf{S}}_I^{\text{in}}, \boldsymbol{\zeta}_I\right)\rangle \\ &= \chi_A^{\rho_{\text{in}}}\left(\left[\sqrt{\eta_{\text{meas}}}\tilde{\zeta}_{S_y^A}, \sqrt{\eta_{\text{meas}}}\tilde{\zeta}_{S_y^B}, \sqrt{\eta_{\text{meas}}}\tilde{\zeta}_{S_x^A}, \sqrt{\eta_{\text{meas}}}\tilde{\zeta}_{S_x^B}, \zeta_{I_y^A}, \zeta_{I_y^B}, \zeta_{I_x^A}, \zeta_{I_x^B}\right]^T\right) \\ &\quad \cdot \exp\left[-\sum_{\{\tilde{\zeta}_i\}} \eta^{\text{pho}}\left(1-\eta^{\text{pre}}\right)|\tilde{\zeta}_i|^2 - \sum_{\{\zeta_i\}}\left(1-\eta^{\text{pho}}\right)|\zeta_i|^2\right] \end{aligned} \tag{3.43}$$

where the scaled $\tilde{\boldsymbol{\zeta}}$ result from the transformation of the beam splitter transformation in Eqn. 3.42:

$$\tilde{\boldsymbol{\zeta}} = \mathbf{B}^\dagger\boldsymbol{\zeta} = \begin{bmatrix} \tilde{\zeta}_{S_y^A} \\ \tilde{\zeta}_{S_y^B} \\ \tilde{\zeta}_{S_x^A} \\ \tilde{\zeta}_{S_x^B} \end{bmatrix} = \frac{1}{\sqrt{2}} \begin{bmatrix} \zeta_{S_y^A} + \zeta_{S_y^B} \\ \zeta_{S_y^A} - \zeta_{S_y^B} \\ \zeta_{S_x^A} + \zeta_{S_x^B} \\ \zeta_{S_x^A} - \zeta_{S_x^B} \end{bmatrix}. \tag{3.44}$$

Rewriting Eqn. 3.43 in terms of $\boldsymbol{\zeta}$, the characteristic function is now

$$\begin{aligned} \chi_A^{\rho_{\text{out}}}(\boldsymbol{\zeta}) = \exp\Big[&-\left(1+\eta_{\text{meas}}\bar{N}\right)\left(|\zeta_{S_y^A}|^2 + |\zeta_{S_x^A}|^2 + |\zeta_{S_y^B}|^2 + |\zeta_{S_x^B}|^2\right) \\ &-\left(1+\bar{N}\right)\left(|\zeta_{I_y^A}|^2 + |\zeta_{I_x^A}|^2 + |\zeta_{I_y^B}|^2 + |\zeta_{I_x^B}|^2\right) \\ &+\tilde{N}\sqrt{2\eta_{\text{meas}}}\Big[\text{Re}\left(\zeta_{S_x^A}\zeta_{I_y^A}\right) + \text{Re}\left(\zeta_{S_x^B}\zeta_{I_y^A}\right) - \text{Re}\left(\zeta_{S_y^A}\zeta_{I_x^A}\right) - \text{Re}\left(\zeta_{S_y^B}\zeta_{I_x^A}\right) \\ &+\text{Re}\left(\zeta_{S_x^A}\zeta_{I_y^B}\right) - \text{Re}\left(\zeta_{S_x^B}\zeta_{I_y^B}\right) - \text{Re}\left(\zeta_{S_y^A}\zeta_{I_x^B}\right) + \text{Re}\left(\zeta_{S_y^B}\zeta_{I_x^B}\right)\Big]\Big]. \end{aligned} \tag{3.45}$$

A useful property of Gaussian antinormally-ordered characteristic functions is that they can be renormalized into a probability density function, whose moments can be calculated.

We find the heralding probability and fidelity by re-expressing Eqn. 3.45 as

$$\chi_A^{\rho_{\text{out}}}(\boldsymbol{\zeta}) = \frac{\pi^8 p_{\mathbf{Z}}(\boldsymbol{\zeta})}{D_1} \tag{3.46}$$

where $p_{\mathbf{Z}}(\boldsymbol{\zeta})$ is the probability density function for a zero-mean Gaussian random vector $\boldsymbol{\zeta}$ with covariance matrices

$$\langle \boldsymbol{\zeta}\boldsymbol{\zeta}^\dagger \rangle = \frac{1}{D_1}\begin{bmatrix} \left(1+\eta_{\text{meas}}\bar{N}\right)\mathbf{I}_{4\times 4} & \mathbf{0}_{4\times 4} \\ \mathbf{0}_{4\times 4} & \left(1+\bar{N}\right)\mathbf{I}_{4\times 4} \end{bmatrix} \quad \langle \boldsymbol{\zeta}\boldsymbol{\zeta}^T \rangle = \frac{1}{D_1}\begin{bmatrix} \mathbf{0}_{4\times 4} & \mathbf{N}_{4\times 4} \\ \mathbf{N}_{4\times 4}^T & \mathbf{0}_{4\times 4} \end{bmatrix} \tag{3.47}$$

for

$$\mathbf{N}_{4\times 4} = \tilde{N}\sqrt{2\eta_{\text{meas}}}\begin{bmatrix} 0 & 0 & -1 & -1 \\ 0 & 0 & -1 & 1 \\ 1 & 1 & 0 & 0 \\ 1 & -1 & 0 & 0 \end{bmatrix} \tag{3.48}$$

and determinant $D_1 = \left(1+\eta_{\text{meas}}\bar{N}\right)^4\left(1+\bar{N}\right)^4 - 256\tilde{N}^8\eta_{\text{meas}}^4$. The output density operator of the Stokes field can be expressed as the operator-valued Fourier transformation of Eqn. 3.45:

$$\begin{aligned}\hat{\rho}_{\text{out}} = &\int \prod_{i=x,y} \frac{d^2\zeta_{I_i^A}}{\pi^2}\frac{d^2\zeta_{I_i^B}}{\pi^2} D_N\left(\hat{S}_{I_i^A}, \zeta_{I_i^A}\right) D_N\left(\hat{S}_{I_i^B}, \zeta_{I_i^B}\right) \\ &\cdot \int \prod_{i=x,y} \frac{d^2\zeta_{S_i^A}}{\pi^2}\frac{d^2\zeta_{S_i^B}}{\pi^2} \chi_A^{\rho_{\text{out}}}(\boldsymbol{\zeta}) D_N\left(\hat{a}'_{S_i^A}, \zeta_{S_i^A}\right) D_N\left(\hat{a}'_{S_i^B}, \zeta_{S_i^B}\right),\end{aligned} \tag{3.49}$$

where $D_N(\hat{a}_i, \zeta_i) = e^{-\zeta_i \hat{a}_i^\dagger} e^{\zeta_i^* \hat{a}_i}$ is the normally-ordered displacement operator. To perform trace operations on the operator-valued Fourier transform in Eqn. 3.49, we know that

$$\langle 0| D_N(\hat{a}_i, \zeta_i) |0\rangle = 1 \qquad \langle 1| D_N(\hat{a}_i, \zeta_i) |1\rangle = 1 - |\zeta_i|^2 \tag{3.50}$$

and that

$$\text{tr}\left[D_N(\hat{a}_i, \zeta_i)\right] = \pi\delta(\zeta_i) \qquad \text{tr}\left[D_N(\hat{a}_i, \zeta_i)\left(\hat{I} - |0\rangle\langle 0|\right)\right] = \pi\delta(\zeta_i) - 1. \tag{3.51}$$

Performing trace operations on the $\hat{a}_i$ mode of an output density operator is equivalent to

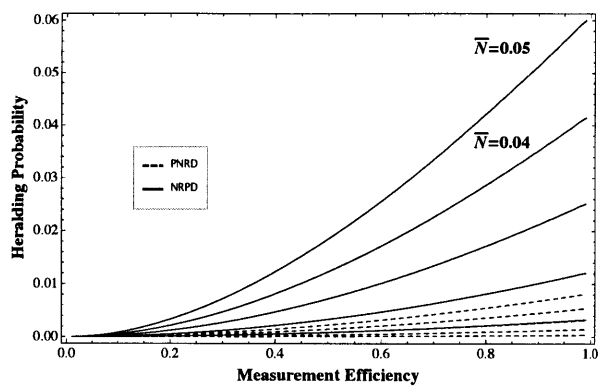

(a) Heralding probability.

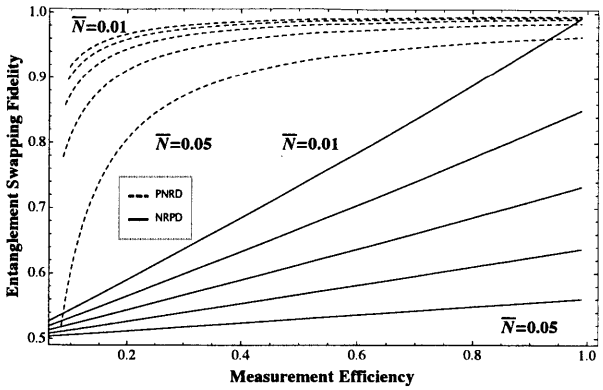

(b) Fidelity of entanglement.

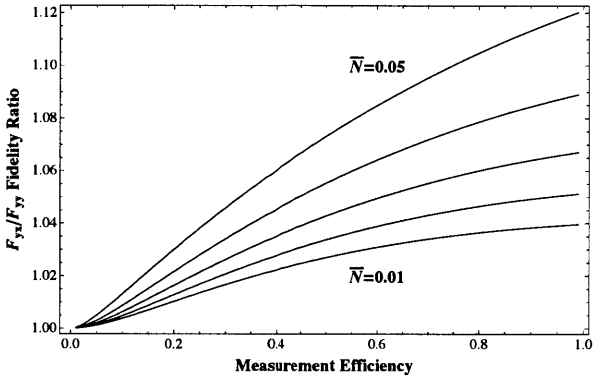

(c) Fidelity ratio for cross- and co-polarized heralding events.

Figure 3-9: Figures of merit for Gaussian state entanglement connection (PNRD and NRPD) for $\bar{N} = 0.01 - 0.05$ $(\Delta N = 0.01)$.

setting $\zeta_i = 0$ in its characteristic function, so any Gaussian moment calculations in the following may involve a marginal distribution of that specified by Eqn. 3.47.

We will first consider the particular case of a $\mathbf{y}-$polarized click at D_A and a $\mathbf{x}-$polarized click at D_B, and then extrapolate to other possibilities: a $\mathbf{x}-$polarized click at D_A and a $\mathbf{y}-$polarized click at D_B, and co-polarized clicks at both D_A and D_B. Applying these trace identities in a PNRD scheme, the post-measurement state of the ensembles is

$$\hat{\rho}^{yx}_{\text{post}} = \frac{1}{P^{yx}_{\text{herald}}} \int \prod_{i=x,y} \frac{d^2\zeta_{I_i^A}}{\pi^2} \frac{d^2\zeta_{I_i^B}}{\pi^2} D_N\left(\hat{S}_{I_i^A}, \zeta_{I_i^A}\right) D_N\left(\hat{S}_{I_i^B}, \zeta_{I_i^B}\right)$$
$$\cdot \int \frac{d^2\zeta_{S_y^A}}{\pi^2} \frac{d^2\zeta_{S_x^B}}{\pi^2} \chi_A^{\rho_{\text{out}}}(\boldsymbol{\zeta}) \left(1 - |\zeta_{S_y^A}|^2\right) \left(1 - |\zeta_{S_x^B}|^2\right), \tag{3.52}$$

where the heralding probability is

$$P_{\text{herald}}^{yx} = \int \frac{d^2\zeta_{S_y^A}}{\pi^2}\frac{d^2\zeta_{S_x^B}}{\pi^2}\chi_A^{\rho_{\text{out}}}\left(\left[\zeta_{S_y^A},\zeta_{S_y^B},\zeta_{S_x^A},\zeta_{S_x^B},0,0,0,0\right]^T\right)\left(1-|\zeta_{S_y^A}|^2\right)\left(1-|\zeta_{S_x^B}|^2\right). \tag{3.53}$$

Applying the Gaussian moment factoring theorem, this heralding probability is

$$\begin{aligned} P_{\text{herald}}^{yx} &= \frac{1}{D_2}\langle\left(1-|\zeta_{S_y^A}|^2\right)\left(1-|\zeta_{S_x^B}|^2\right)\rangle \\ &= \frac{1}{D_2^3}\left[D_2^2 - 2\left(1+\eta_{\text{meas}}\bar{N}\right)D_2 + \left(1+\eta_{\text{meas}}\bar{N}\right)^2\right] \\ &= \frac{\eta_{\text{meas}}^2\bar{N}^2(\eta_{\text{meas}}\bar{N}(\eta_{\text{meas}}\bar{N}+3)+3)^2}{(\eta_{\text{meas}}\bar{N}+1)^{10}}, \end{aligned} \tag{3.54}$$

where $\langle\ \rangle$ denotes ensemble averaging treating $\boldsymbol{\zeta}$ as a complex-valued Gaussian random vector whose probability density function is a marginal distribution of Eqn. 3.47, with $D_2 = \left(1+\eta_{\text{meas}}\bar{N}\right)^4$. Note that the second-moments of the signal modes reaching the photodetectors are all identical, so the heralding probabilities for each of the four heralding probabilities mentioned earlier are equal. Therefore, $P_{\text{herald}} = 4P_{\text{herald}}^{yx}$ for the PNRD case. Applying the trace identities in Eqn 3.51, the post-measurement joint density operator for the NRPD scheme is

$$\begin{aligned} \hat{\rho}_{\text{post}}^{yx} = \frac{1}{P_{\text{herald}}^{yx}}\int\prod_{i=x,y}\frac{d^2\zeta_{I_i^A}}{\pi^2}\frac{d^2\zeta_{I_i^B}}{\pi^2}D_N\left(\hat{S}_{I_i^A},\zeta_{I_i^A}\right)D_N\left(\hat{S}_{I_i^B},\zeta_{I_i^B}\right) \\ \cdot\int\frac{d^2\zeta_{S_y^A}}{\pi^2}\frac{d^2\zeta_{S_x^B}}{\pi^2}\chi_A^{\rho_{\text{out}}}(\boldsymbol{\zeta})\left[\pi\delta\left(\zeta_{S_y^A}\right)-1\right]\left[\pi\delta\left(\zeta_{S_x^B}\right)-1\right]. \end{aligned} \tag{3.55}$$

Tracing out the idler excitation modes, the NRPD heralding probability is

$$P_{\text{herald}}^{yx} = \int\prod_{i=x,y}\frac{d^2\zeta_{S_i^A}}{\pi^2}\frac{d^2\zeta_{S_i^B}}{\pi^2}\chi_A^{\rho_{\text{out}}}\left(\left[\zeta_{S_y^A},\zeta_{S_y^B},\zeta_{S_x^A},\zeta_{S_x^B},0,0,0,0\right]^T\right)\left[\pi\delta\left(\zeta_{S_y^A}\right)-1\right]\left[\pi\delta\left(\zeta_{S_x^B}\right)-1\right], \tag{3.56}$$

which yields

$$P_{\text{herald}}^{yx} = \frac{\eta_{\text{meas}}^2 \bar{N}^2}{(\eta_{\text{meas}} \bar{N} + 1)^4}. \tag{3.57}$$

This PNRD heralding probability and PNRD fidelity, as well as the NRPD heralding probability and fidelity are shown in Fig. 3-9. The results for heralding probability are consistent with our understanding of multiple-excitation effects, as described previously in the context of entanglement distribution in Section 3.2.3: reading from ensembles with a higher average spin excitation $\bar{N}$ will yield more anti-Stokes photons, resulting in a higher likelihood of a heralding event when the photodetectors cannot resolve photon number.

The fidelity, when a **y**-polarized D_A click and a **x**-polarized D_B click provide the herald, is given by

$$\begin{aligned} F_{yx} &= \langle \psi_1 | \, \hat{\rho}_{\text{post}}^{yx} \, | \psi_1 \rangle \\ &= \frac{1}{P_{\text{herald}}^{yx}} \int \prod_{i=x,y} \frac{d^2\zeta_{I_i^A}}{\pi^2} \frac{d^2\zeta_{I_i^B}}{\pi^2} \left[1 - \frac{|\zeta_{I_x^A}\zeta_{I_y^B} - \zeta_{I_y^A}\zeta_{I_x^B}|^2}{2} \right] \\ &\quad \cdot \int \frac{d^2\zeta_{S_y^A}}{\pi^2} \frac{d^2\zeta_{S_x^B}}{\pi^2} \chi_A^{\rho_{\text{out}}}(\boldsymbol{\zeta}) \left(1 - |\zeta_{S_y^A}|^2 \right) \left(1 - |\zeta_{S_x^B}|^2 \right) \\ &= \frac{1}{D_1 P_{\text{herald}}^{yx}} \langle \left(1 - |\zeta_{S_y^A}|^2 \right) \left(1 - |\zeta_{S_x^B}|^2 \right) \left(1 - \frac{|\zeta_{I_x^A}\zeta_{I_y^B} - \zeta_{I_y^A}\zeta_{I_x^B}|^2}{2} \right) \rangle. \end{aligned} \tag{3.58}$$

The necessary higher-order moments for this calculation are, from Gaussian moment

factoring

$$\begin{aligned}
\langle|\zeta_{I_x^A}\zeta_{I_y^B}-\zeta_{I_y^A}\zeta_{I_x^B}|^2\rangle &= \langle|\zeta_{I_x^A}|^2\rangle\langle|\zeta_{I_y^B}|^2\rangle+\langle|\zeta_{I_y^A}|^2\rangle\langle|\zeta_{I_x^B}|^2\rangle \\
\langle|\zeta_{S_y^A}|^2|\zeta_{I_x^A}\zeta_{I_y^B}-\zeta_{I_y^A}\zeta_{I_x^B}|^2\rangle &= \langle|\zeta_{S_y^A}|^2\rangle\langle|\zeta_{I_x^A}|^2\rangle\langle|\zeta_{I_y^B}|^2\rangle+\langle|\zeta_{S_y^A}|^2\rangle\langle|\zeta_{I_y^A}|^2\rangle\langle|\zeta_{I_x^B}|^2\rangle \\
&\quad+|\langle\zeta_{S_y^A}\zeta_{I_x^A}\rangle|^2\langle|\zeta_{I_y^B}|^2\rangle+|\langle\zeta_{S_y^A}\zeta_{I_x^B}\rangle|^2\langle|\zeta_{I_y^A}|^2\rangle \\
\langle|\zeta_{S_x^B}|^2|\zeta_{I_x^A}\zeta_{I_y^B}-\zeta_{I_y^A}\zeta_{I_x^B}|^2\rangle &= \langle|\zeta_{S_x^B}|^2\rangle\langle|\zeta_{I_x^A}|^2\rangle\langle|\zeta_{I_y^B}|^2\rangle+\langle|\zeta_{S_x^B}|^2\rangle\langle|\zeta_{I_y^A}|^2\rangle\langle|\zeta_{I_x^B}|^2\rangle \\
&\quad+|\langle\zeta_{S_x^B}\zeta_{I_y^B}\rangle|^2\langle|\zeta_{I_x^A}|^2\rangle+|\langle\zeta_{S_x^B}\zeta_{I_y^A}\rangle|^2\langle|\zeta_{I_x^B}|^2\rangle \\
\langle|\zeta_{S_y^A}|^2|\zeta_{S_x^B}|^2|\zeta_{I_x^A}\zeta_{I_y^B}-\zeta_{I_y^A}\zeta_{I_x^B}|^2\rangle &= \langle|\zeta_{S_y^A}|^2\rangle\langle|\zeta_{S_x^B}|^2\rangle\langle|\zeta_{I_x^A}|^2\rangle\langle|\zeta_{I_y^B}|^2\rangle \\
&\quad+\langle|\zeta_{S_y^A}|^2\rangle\langle|\zeta_{S_x^B}|^2\rangle\langle|\zeta_{I_y^A}|^2\rangle\langle|\zeta_{I_x^B}|^2\rangle \\
&\quad+|\langle\zeta_{S_y^A}\zeta_{I_x^A}\rangle|^2|\langle\zeta_{S_x^B}\zeta_{I_y^B}\rangle|^2+|\langle\zeta_{S_y^A}\zeta_{I_x^B}\rangle|^2|\langle\zeta_{S_x^B}\zeta_{I_y^A}\rangle|^2 \\
&\quad+|\langle\zeta_{S_y^B}\zeta_{I_x^A}\rangle|^2\langle|\zeta_{S_x^B}|^2\rangle\langle|\zeta_{I_y^B}|^2\rangle+|\langle\zeta_{S_y^A}\zeta_{I_x^B}\rangle|^2\langle|\zeta_{S_x^B}|^2\rangle\langle|\zeta_{I_y^B}|^2\rangle \\
&\quad+|\langle\zeta_{S_x^B}\zeta_{I_y^B}\rangle|^2\langle|\zeta_{I_x^A}|^2\rangle\langle|\zeta_{S_y^A}|^2\rangle+|\langle\zeta_{S_x^B}\zeta_{I_y^A}\rangle|^2\langle|\zeta_{S_y^A}|^2\rangle\langle|\zeta_{I_x^B}|^2\rangle \\
&\quad-\Big[\langle\zeta_{S_y^A}\zeta_{I_x^A}\rangle\langle\zeta^*_{S_y^A}\zeta^*_{I_x^B}\rangle\langle\zeta_{S_x^B}\zeta_{I_y^B}\rangle\langle\zeta^*_{S_x^B}\zeta^*_{I_y^A}\rangle \\
&\qquad+\langle\zeta_{S_y^A}\zeta_{I_x^B}\rangle\langle\zeta^*_{S_y^A}\zeta^*_{I_x^A}\rangle\langle\zeta_{S_x^B}\zeta_{I_y^A}\rangle\langle\zeta^*_{S_x^B}\zeta^*_{I_y^B}\rangle\Big] \qquad (3.59)
\end{aligned}$$

Applying the covariance matrix in Eqn. 3.47 to these higher-order moment expressions, the PNRD fidelity is given by

$$\begin{aligned}
F_{yx} = \Bigg[&\frac{1}{D_1^3}\left[D_1^2-2\left(1+\eta_{\text{meas}}\bar{N}\right)1_2+\left(1+\eta_{\text{meas}}\bar{N}\right)^2\right] \\
&-\frac{1}{2D_1}\left(\frac{2\left(1+\bar{N}\right)^2}{D_1^2}-\frac{4\left(1+\eta_{\text{meas}}\bar{N}\right)\left(1+\bar{N}\right)^2+8\eta\left(1+\bar{N}\right)\tilde{N}^2}{D_1^3}\right. \\
&\left.+\frac{2\left(1+\eta_{\text{meas}}\bar{N}\right)^2\left(1+\bar{N}\right)^2+8\eta\tilde{N}^2\left(1+\eta_{\text{meas}}\bar{N}\right)\left(1+\bar{N}\right)}{D_1^4}\right)\Bigg]. \qquad (3.60)
\end{aligned}$$

The F_{xy} fidelity is easily seen to be the same as the F_{yx} fidelity, as in the heralding probability calculation presented earlier. While the F_{xx} and F_{yy} fidelities will also equal, they will differ from the cross-polarized fidelities. To find F_{yy}, we need to evaluate

$$F_{yy}=\frac{1}{D_1P_{\text{herald}}^{yy}}\langle\left(1-|\zeta_{S_y^A}|^2\right)\left(1-|\zeta_{S_y^B}|^2\right)\left(1-\frac{|\zeta_{I_x^A}\zeta_{I_y^B}-\zeta_{I_y^A}\zeta_{I_x^B}|^2}{2}\right)\rangle. \qquad (3.61)$$

The calculation is identical to that for F_{yx} save for the eighth-order moment, which factors into

$$\begin{aligned}
&\langle|\zeta_{S_y^A}|^2|\zeta_{S_y^B}|^2|\zeta_{I_x^A}\zeta_{I_y^B}-\zeta_{I_y^A}\zeta_{I_x^B}|^2\rangle = \\
&\quad\langle|\zeta_{S_y^A}|^2\rangle\langle|\zeta_{S_y^B}|^2\rangle\langle|\zeta_{I_x^A}|^2\rangle\langle|\zeta_{I_y^B}|^2\rangle+\langle|\zeta_{S_y^A}|^2\rangle\langle|\zeta_{S_y^B}|^2\rangle\langle|\zeta_{I_y^A}|^2\rangle\langle|\zeta_{I_x^B}|^2\rangle \\
&\qquad+|\langle\zeta_{S_y^B}\zeta_{I_x^A}\rangle|^2\langle|\zeta_{S_y^A}|^2\rangle\langle|\zeta_{I_y^B}|^2\rangle+|\langle\zeta_{S_y^A}\zeta_{I_x^A}\rangle|^2\langle|\zeta_{S_y^B}|^2\rangle\langle|\zeta_{I_y^B}|^2\rangle \\
&\qquad+|\langle\zeta_{S_y^A}\zeta_{I_x^B}\rangle|^2\langle|\zeta_{I_y^A}|^2\rangle\langle|\zeta_{S_y^B}|^2\rangle+|\langle\zeta_{S_y^B}\zeta_{I_x^B}\rangle|^2\langle|\zeta_{S_y^A}|^2\rangle\langle|\zeta_{I_y^A}|^2\rangle. \qquad (3.62)
\end{aligned}$$

Comparing Eqn. 3.62 and 3.59, it immediately becomes obvious that the F_{yy} and F_{yx} differ in their contribution to the overall entanglement fidelity. Prior to our Gaussian state analysis, we assumed that ensembles A and B had loaded pure singlet states prior to entanglement swapping. Their pure singlet states yield a perfect fidelity in both NRPD and PNRD photodetection schemes with the heralding of cross-polarized photons at detectors D_A and D_B. However, the measurement of co-polarized photons is indistinguishable from a cross-polarized photon measurement, even though entanglement need not be successfully swapped when the herald comes from co-polarized photons. As such, we define the fidelity of entanglement as

$$F_E=\frac{P_{\text{success}}}{P_{\text{herald}}}=\frac{2P_{\text{herald}}^{yx}F_{yx}+2P_{\text{herald}}^{yy}F_{yy}}{P_{\text{herald}}}. \qquad (3.63)$$

Figs. 3-9(b) and 3-9(c) show the fidelity of entanglement following a swapping operation. As in polarization entanglement distribution, reading and producing multiple-excitations increases heralding probability at the expense of the entanglement fidelity. In this regard, the fidelity plots for emphasize some significant differences between the PNRD and NRPD cases. From the post-measurement density operator, this NRPD fidelity is given by

$$\begin{aligned}
F_{yx}&=\langle\psi_1|\,\hat{\rho}_{\text{post}}^{yx}\,|\psi_1\rangle \\
&=\frac{1}{P_{\text{herald}}^{yx}}\int\prod_{i=x,y}\frac{d^2\zeta_{I_i^A}}{\pi^2}\frac{d^2\zeta_{I_i^B}}{\pi^2}\left[1-\frac{|\zeta_{I_x^A}\zeta_{I_y^B}-\zeta_{I_y^A}\zeta_{I_x^B}|^2}{2}\right] \\
&\quad\cdot\int\frac{d^2\zeta_{S_y^A}}{\pi^2}\frac{d^2\zeta_{S_x^B}}{\pi^2}\chi_A^{\rho_{\text{out}}}(\zeta)\left[\pi\delta\left(\zeta_{S_y^A}\right)-1\right]\left[\pi\delta\left(\zeta_{S_x^B}\right)-1\right]. \qquad (3.64)
\end{aligned}$$

Unlike the difference in moment factoring present in the PNRD fidelity calculation, the NRPD fidelity is identical for to cross-polarized and co-polarized photodetection events, as is evident from the NRPD POVM applied in Eqn. 3.64. This calculation is only dependent on the second-moments of the idler ensembles and the normalizations inherent in the marginal probability distributions following photodetection, each of which is independent of photon polarization. Equation 3.64 thus simplifies to

$$F_{yx} = \frac{1}{P^{yx}_{\text{herald}}}\left[\frac{(\bar{N}+1)^6(\eta_{\text{meas}}\bar{N}+1)^7 - 2(\bar{N}+1)^6(\eta_{\text{meas}}\bar{N}+1)^6 + 1}{(\bar{N}+1)^{10}(\eta_{\text{meas}}\bar{N}+1)^9} + \frac{1}{D_1} - \frac{\left(\bar{N}+1\right)^2}{D_1^3}\right], \tag{3.65}$$

which is plotted in Fig. 3-9(b). The PNRD case lets us actively discard garbage photodetection events that might result from multiple-excitations present at entanglement distribution. In this case, we know that having matching, *single* counts at D_A and D_B will very likely correspond to a successful entanglement swapping operation with photon-number resolving detectors. On the other hand, high $\bar{N}$, even in the presence of high measurement efficiency, severely affects our NRPD entanglement fidelity, because NRPD cannot distinguish false heralding events. Also surprising is the ratio of the fidelity of entanglement for cross-polarized and co-polarized photodetection events, as shown in Fig. 3-9(c). These fidelities are very close to each other, although they begin to diverge as $\bar{N}$ increases. That they are so close in value is somewhat surprising because cross-polarized photodetection was predicted for unity entanglement fidelity in the case of a pure singlet distribution, whereas co-polarized photodetection would not necessarily be indicative of a singlet state remaining in the idler ensembles.

Chapter 4

Conclusions

To date, the theoretical progress of quantum information science and engineering has surpassed its experimental achievements. This thesis paints a detailed picture of what future long-distance quantum communication networks might look like, and their limitations. In the course of this work, we have analyzed quantum networks that distribute polarization entanglement using neutral atomic ensembles. This analysis focuses on three areas. We first abstracted quantized light-ensemble interactions within a heralding atomic memory and determined that these interactions preclude a Gaussian state analysis of local entanglement distribution (Chapter 2, Appendix A). After describing the potential losses in an entanglement distribution architecture, we applied the SU (2) representation of beam splitter operators to model loss in a number state basis, and performed a Gaussian state analysis of polarization entanglement swapping (Chapter 3). A number-state analysis of the entanglement distribution captures the joint state of the heralding light and atomic excitations, accounting for imperfections in transmission loss, photodetection efficiency and counting resolution, and multiple-pair events at the downconversion source.

The numerical characterization of entanglement distribution and connection presented in this thesis is so far consistent with our physical intuition of how such networks should behave. In particular, the probability of a successful heralding event is independent of whether a single, significant, uniform efficiency loss is located either before or after an ensemble memory, or during photodetection. With regards to the probability measuring a single photon, all losses are effectively the same. The same is not true for fidelity. A uniform transmission

loss between the entanglement source and the ensembles will significantly reduce the likelihood that you've stored a polarization Bell state, but significant quantum efficiency losses at photodetection are less likely to diminish that fidelity. Increasing the pump power at the entanglement source increases the likelihood of multiple-pair events, increasing the heralding probability but making the fidelity more sensitive to transmission and photodetection efficiency losses. These results are true for both number-resolving and non-resolving photodetectors. For both entanglement distribution and connection, heralding probabilities for non-resolving detectors are higher, but the fidelities are significantly lower. Many of these same issues appear in entanglement swapping as well.

Two areas in this thesis are particularly ripe for extension and exploration: further investigation into the mechanisms and imperfections of ensemble memories that distribute polarization entanglement, and formalizing the number state analysis of systems with loss-modeling beam splitters. Several possible extensions are relatively straightforward, such as the inclusion of phase offsets between orthogonally-polarized paths in during entanglement distribution. Others require a more careful consideration of the underlying physics of quantum memories. For example, the performance analysis of polarization entanglement distribution presented in this thesis omits the presence of spin decoherence in the atomic ensembles. In quantifying the singlet-storage fidelity, there is a tradeoff between the time scale of decoherence of Dicke excitations, the time it takes for a single heralding photon to reach a photodetector, and the post-memory transmission efficiency (which scales with the post-transmission length). Spin decoherence of the ensemble may therefore be a significant factor limiting the optimal physical distance that local entanglement distribution can cover. Another possible departure would be to discard the DLCZ approach entirely, using a stimulated Raman or EIT approach, instead of a spontaneous Raman process. The Hamiltonian in this approach would be amenable to a traditional Gaussian state analysis, and would allow for deterministic control of read and write processes in entanglement distribution. As of the writing of this thesis, however, there is currently no accepted means of nondestructive verification of successful entanglement distribution in a coherently-controlled Λ-level atomic ensemble. This open problem makes certain long-distance quantum communication tasks, such as repeated entanglement connection, difficult to accomplish using a driven Raman

process.

Unrelated to the question of memories is formalizing the architectural analysis of loss-modeling beam splitters. The SU (2) number-state representation for *single* beam splitters is discussed in great detail by [CST89]. Summation compositions of beam splitter coefficients determined important architectural figures of merit—heralding probability, fidelity, and success probability—in the course of this work, but were calculated numerically. With a number-state basis, what general properties or figures of merit of a quantum network can we determine if we limit ourselves to linear optical elements (e.g., 50-50 and polarizing beam splitters, loss elements), photodetectors, and photon-number conserving nonlinear optical elements (e.g., heralding quantum memories or Kerr crystals)? In particular, do any of the properties of a beam splitter coefficient introduced in Chapter 3 permit any useful, analytical simplifications when using the joint density operator of a network to calculate a figure of merit? Is a number-state analysis consistent with a SPDC Gaussian state analysis when nonlinear elements are excluded and we are limited entirely to the propagation of optical fields? Answers to these questions could possibly alleviate the exhausting notational and computational difficulties currently necessitated by number-state analysis.

Appendix A

Numerical Simulations for Quantum Memory Interaction Hamiltonian

In Section 3.2.2, we discussed the dynamics of a trilinear Hamiltonian and applied an anzatz solution assuming unity heralding probability to our architectural analysis. In the following, we provide a model for the trilinear Hamiltonian's dynamics in the presence of cavity loss and spontaneous emission, and use a quantum Monte Carlo simulation of this model to empirically justify our anzatz.

In Chapter 2, we abstracted a model for the interaction of input quantum field into an ensemble-based quantum memory. A basis for this model is inspired by recent experimental work on heralded single-photon atomic memories and interfaces from [STTVac07] [TGS+09], which utilized two spatially-overlapping atomic ensembles to absorb arbitrarily polarized single photons. Heralding was observed (at rate of 10^{-6}, using pulsed coherent states ($\bar{N} \approx 500$) with an absorption probability $\alpha = 0.01$. Despite operating in an effective single-photon regime, multiple photon inputs were still present, a problem we wish to analyze in the case of a parametric downconverter input. We consider an ensemble of Λ-type atoms confined in a single-sided, low-finesse ring cavity, as shown in Fig. 2-1. The $|g\rangle - |e\rangle$ and $|e\rangle - |s\rangle$ transitions are coupled to the cavity modes $\hat{a}$ and $\hat{b}$, respectively, each with coupling coefficient g_c. Under the rotating wave approximation, the interaction Hamiltonian for the

collective interaction process is given by

$$\hat{H} = \hbar\Gamma\left(\hat{a}\hat{S}^{\dagger}\hat{b}^{\dagger} + \hat{b}\hat{S}\hat{a}^{\dagger}\right) \tag{A.1}$$

where $\Gamma = g_c^2 N_a/\Delta$ (Δ is the detuning from the two-photon resonance). The input output expressions for single-sided optical cavities with decay rate κ and input states $\hat{a}_{\text{in}}$ (downconverter) and $\hat{b}_{\text{in}}$ (in vacuum) are

$$\begin{aligned}\hat{a}_{\text{out}}(t) &= \sqrt{\kappa_a}\hat{a}(t) - \hat{a}_{\text{in}}(t)\\ \hat{b}_{\text{out}}(t) &= \sqrt{\kappa_b}\hat{b}(t) - \hat{b}_{\text{in}}(t),\end{aligned} \tag{A.2}$$

and the Eqn.s of motion for the internal state operators are,

$$\begin{aligned}\frac{d\hat{a}}{dt} &= -i\Gamma\hat{S}\hat{b} - \frac{\kappa}{2}\hat{a} + \sqrt{\kappa}\hat{a}_{\text{in}}(t)\\ \frac{d\hat{b}}{dt} &= -i\Gamma\hat{S}^{\dagger}\hat{a} - \frac{\kappa}{2}\hat{b} + \sqrt{\kappa}\hat{b}_{\text{in}}(t)\\ \frac{d\hat{S}^{\dagger}}{dt} &= i\Gamma\hat{b}\hat{a}^{\dagger}.\end{aligned} \tag{A.3}$$

In principle, Eqns. A.2 and A.3 are all that are needed to determine $\hat{a}_{\text{out}}(t)$ and $\hat{b}_{\text{out}}(t)$. Including the spontaneous emission γ of the excited state $|e\rangle$, we can alternatively solve for the dynamics of expected values of these modes by numerically integrating the master Eqn. for the density state $\hat{\rho}$:

$$\frac{d\hat{\rho}}{dt} = i\left[\hat{\rho}, \hat{H}_{\text{int}}\right] + \left(2\kappa_a\mathcal{D}\left[\hat{a}\right] + 2\kappa_b\mathcal{D}\left[\hat{b}\right] + \gamma\mathcal{D}\left[\hat{S}\right]\right)\hat{\rho}, \tag{A.4}$$

where

$$\mathcal{D}\left[\hat{a}\right]\hat{\rho} = \hat{a}\hat{\rho}\hat{a}^{\dagger} - \frac{1}{2}\hat{a}^{\dagger}\hat{a}\hat{\rho} - \frac{1}{2}\hat{\rho}\hat{a}^{\dagger}\hat{a} \tag{A.5}$$

is a superoperator that describes cavity and spontaneous emission losses by mixing each mode with a zero-temperature bath of harmonic oscillators. This approach assumes that $\hat{\rho}(0^{+}) = \hat{\rho}_{\text{in}}$. For this particular problem, the joint Hilbert space of three boson modes is quite large, and using the limited memory available, the simulation was was carried out in

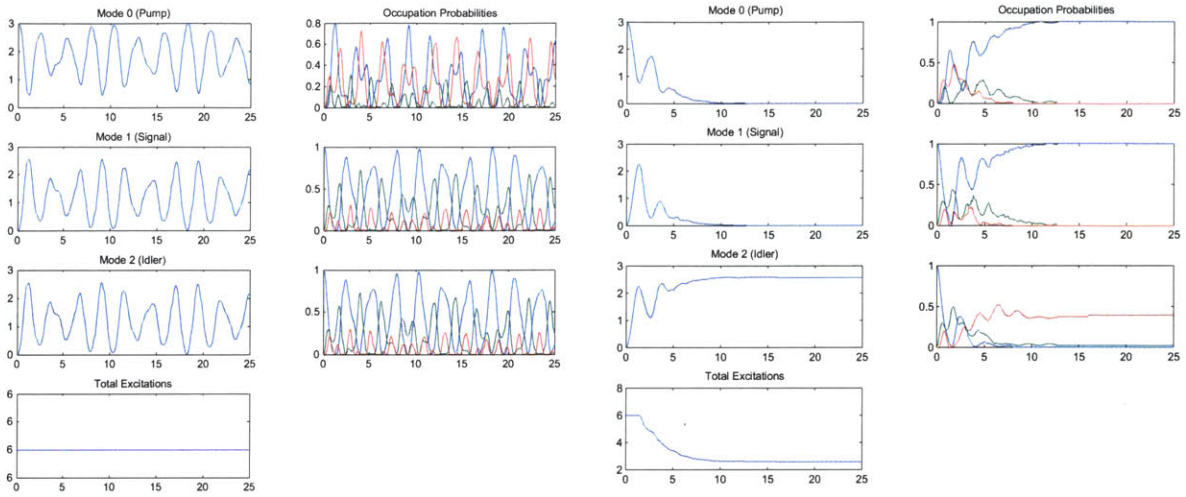

(a) No loss ($g_c = 5$, $\kappa_a = \kappa_b = \gamma = 0$).

(b) Including cavity and ensemble spontaneous emission losses ($g_c = 5$, $\kappa_a = 0.2$, $\kappa_b = 2$, and $\gamma = 0.01$).

Figure A-1: Photon-number expectation values for $\hat{a}$ (pump), $\hat{b}$ (signal), and $\hat{S}$ (idler) starting with $|n(0^+)\rangle_a = |3\rangle_a$, averaged for 50 simulations. For each mode, occupation probabilities are given for the ground (blue), first excited (green), and second excited (red) states.

the Schrodinger picture using an effective dissipative Hamiltonian

$$\hat{H}_{\text{eff}} = \hat{H}_{\text{int}} - \frac{i}{2}\left(2\kappa_a \hat{a}^\dagger \hat{a} + 2\kappa_b \hat{b}^\dagger \hat{b} + \gamma \hat{S}^\dagger \hat{S}\right). \tag{A.6}$$

Fig. A-1 shows the simulated dynamics of a three-photon Fock state in a pump mode interacting with an cavity-confined ensemble. In the absence of loss (Fig. A-1(a)), the expectation value of the three modes oscillate, conserving the total expected photon number. Even in the absence of loss, the pump photons are not completely converted to ensemble excitations and heralding photons, possibly because of quantum noise [GALS07]. The introduction of loss (Fig. A-1(b)) shows that it is possible load a Fock state during an initial time interval, leading behind an idler ensemble excitation, and collecting the heralding photons leaking out of the cavity.

A.1 Analytical Dynamical and Trilinear Hamiltonians

In general, a Hamiltonian that cannot be analytically diagonalized will not have analytical dynamics [BR97, KC09], and will therefore not be useful in a Gaussian state analysis. A three-mode interaction describes a heralding quantum memory where an input quantum field (pump mode $\hat{a}$) creates a stationary ensemble excitation (idler mode $\hat{b}$) and a heralding Stokes photon (signal mode $\hat{S}$). Parameterizing the strength of this interaction by Γ, the trilinear Hamiltonian describing this process is then

$$\hat{H} = \hat{H}_0 + \hat{H}_{\text{int}} \tag{A.7}$$

where

$$\hat{H}_0 = \omega_a \hat{a}^\dagger \hat{a} + \omega_b \hat{b}^\dagger \hat{b} + \omega_S \hat{S}^\dagger \hat{S} \tag{A.8}$$

$$\hat{H}_{\text{int}} = \Gamma \hat{a} \hat{b}^\dagger \hat{S}^\dagger + \Gamma^* \hat{S} \hat{b} \hat{a}^\dagger \tag{A.9}$$

with

$$\left[\hat{H}_0, \hat{H}_{\text{int}}\right] = 0. \tag{A.10}$$

There are underlying SU (2) and SU (1, 1) symmetries of this Hamiltonian because the following operators are invariant under time evolution:

$$\begin{aligned} \hat{N}_{ab} &= \hat{a}^\dagger \hat{a} + \hat{b}^\dagger \hat{b} \\ \hat{N}_{aS} &= \hat{a}^\dagger \hat{a} + \hat{S}^\dagger \hat{S} \\ \hat{N}_{bS} &= \hat{b}^\dagger \hat{b} - \hat{S}^\dagger \hat{S}. \end{aligned} \tag{A.11}$$

Only two of these are linear independent, as $\hat{N}_{ab} - \hat{N}_{aS} = \hat{N}_{bS}$, and, assuming that each mode begins from rest, we can also say that

$$\hat{N}_{abc} = 2\hat{a}^\dagger \hat{a} + \hat{b}^\dagger \hat{b} + \hat{S}^\dagger \hat{S} \qquad \hat{N}_{bc} = \hat{b}^\dagger \hat{b} - \hat{S}^\dagger \hat{S} \tag{A.12}$$

are conserved quantities. Choosing $\omega_b = \omega_S = \omega_a/2$, Eqn. A.7 can be written (up to a constant) as

$$\hat{H} = \omega_a \left(\hat{a}^\dagger \hat{a} + \hat{K}_0\right) + \Gamma \hat{a} \hat{K}_+ + \Gamma^* \hat{a}^\dagger \hat{K}_-, \tag{A.13}$$

where $\hat{K}_\pm$ are the operators spanning the SU$(1,1)$ Lie algebra. The trilinear Hamiltonian expressed in terms of its Lie group symmetries is not analytically diagonalizable because its terms are not bilinear, and therefore do not form a finite-dimensional Lie algebra (a non-negotiable requirement for diagonalization) [BR97, KC09].

A.2 Code for Numerical Calculations

Eqn. A.4 was simulated[1] using the Quantum Optics Toolbox for Matlab 5[2], modified from pre-existing sample source provided by Paul D. Nation [Tan99, NB10]. The QOToolbox bridges high-level symbolic representations and numerical calculations in quantum optics rather seamlessly, and is good for quickly bypassing a laborious calculation to build physical intuition. This code generates graphs of expectation values for modes $\hat{a}$, $\hat{b}$, and $\hat{S}$ on a truncated Fock space with $n = 11$, assuming a three-photon Fock state input to the $\hat{a}$ mode and all other modes starting at rest.

```
function [] = run_new_mc()
% Quantum Monte-Carlo simulation of a trilinear Hamiltonian
% Input field: harmonic oscillator initially in Fock or
% squeezed state.
% Modes interact with thermal bath to simulate
% open-quantum system loss.
%
% Modified by Bhaskar Mookerji (mookerji@mit.edu)
% from the original author:
%  Paul D. Nation 2010 (Dartmouth College),
%  paul.d.nation@dartmouth.edu

N0=11;
```

[1] Simulated with Matlab 7.11.0.584 (R2010b) using a 2.4GHz Intel Core2Duo MacBook Pro 7.1, 4GB 1067MHz DD3 memory.

[2] Original source at `http://qwiki.stanford.edu/index.php/Quantum_Optics_Toolbox`. Packaged for Mac OS X by Paul D. Nation at `http://dml.riken.jp/~paul/page5/index.html`.

```
N1=11; %number of basis states for first mode
N2=N1; %number of basis states for second mode
K=2; %value of parametric coupling strength (rate)
gamma0=0.00;
gamma1=0.00;
gamma2=0.0;
alpha=sqrt(3);%coherent state amplitude
epsilon=0.5i; %squeezing parameter
tfinal=10.0;
dt=0.02;
tlist=0:dt:tfinal; %evaluation times for evaluating differential equation
taulist=K.*tlist;
ntraj=1; %number of trajectories to run

%defining lowering operators
a0=tensor(destroy(N0),identity(N1),identity(N2));
a1=tensor(identity(N0),destroy(N1),identity(N2));
a2=tensor(identity(N0),identity(N1),destroy(N2));

p=(a1-1i*a2);

%define number oeprators for modes 0->2
num0=a0*a0;
num1=a1*a1;
num2=a2*a2;
%dissipative operators for zero-temp. bath
C0=sqrt(2*gamma0)*a0;
C1=sqrt(2*gamma1)*a1;
C2=sqrt(2*gamma2)*a2;

%inital state for system: coherent state for mode 0 and vacuum for 1&2
vacuum=tensor((basis(N0,1)),basis(N1,1),basis(N2,1));
D=expm(alpha*a0-conj(alpha)*a0); %mode 0 displacement operator
S=expm(0.5*conj(epsilon)*a0^2-0.5*epsilon*(a0)^2);
%D=1;
%S=1;
%initial_state=a0*a0*a0*vacuum;
initial_state=S*vacuum;

%Wigner function variables
% psi0=ptrace(initial_state,1);
xvec = [-100:100]*10/100; yvec = xvec;
% W = wfunc(psi0,xvec,yvec,1);
% f1 = figure(1); pcolor(xvec,yvec,real(W));
% colorbar;
```

```
% shading interp; title(Wigner function of squeezed state);


%interaction picture Hamiltonian
H=1i*K*(a0*a1*a2-a0*a1*a2);

%effective non-unitary Hamiltonian (includes losses)
Heff=H-0.5*1i*((C0*C0)+(C1*C1)+(C2*C2));

% %options for solver (needed to prevent error accumulation)
options.lmm=BDF;
options.iter=NEWTON;
options.mxstep=100000;
options.reltol=1e-6;
options.abstol=1e-6;

%call to monte-carlo solver
mc2file(test.dat,-1i*Heff,{C0,C1,C2},{},initial_state,tlist,ntraj,options);
mcsolve(test.dat,out.dat,clix.dat);
fid=fopen(out.dat,rb); %open data file

%init. arrays for expectation values of num. oper. at tlist times
photon_num0=zeros(1,length(tlist));
photon_num1=zeros(1,length(tlist));
photon_num2=zeros(1,length(tlist));

%init matricies for prob. of nth num. state at times tlist
Pn0=zeros(N0,length(tlist));
Pn1=zeros(N1,length(tlist));
Pn2=zeros(N2,length(tlist));

variance=zeros(1,length(tlist));
statepump=zeros(1,length(tlist));
statesignal=zeros(1,length(tlist));
expec0=zeros(1,N0);

for k=1:ntraj
   if gettraj(fid)≠k, error(Unexpected data in file); end
   psi=qoread(fid,dims(initial_state),size(tlist)); %readout state vectors at eval times
   %expectation values of number operator in modes 0->2
   photon_num0=photon_num0+expect(num0,psi)./norm(psi).^2;
   photon_num1=photon_num1+expect(num1,psi)./norm(psi).^2;
   photon_num2=photon_num2+expect(num2,psi)./norm(psi).^2;
   %calculate avg. probability of being in n-th number state at tlist times
   for j=1:length(tlist)
```

```
        p0=ptrace(psi{j},1)/trace(ptrace(psi{j},1));
        p1=ptrace(psi{j},2)/trace(ptrace(psi{j},2));
        p2=ptrace(psi{j},3)/trace(ptrace(psi{j},3));
        p12=ptrace(psi{j},[2,3])/trace(ptrace(psi{j},[2,3]));
        elems0=diag(full(p0(:,:)));
        elems1=diag(full(p1(:,:)));
        elems2=diag(full(p2(:,:)));
        for p=1:N0
           if sum(elems0(1:p))>0.99
              statepump(j)=p;
              break
           end
        end
        for s=1:N1
           if sum(elems1(1:s))>0.99
              statesignal(j)=s;
              break
           end
        end
        Pn0(:,j)=Pn0(:,j)+elems0(:); %distribution of pump over number states
        Pn1(:,j)=Pn1(:,j)+elems1(:); %distribution of mode 1 over number states
        Pn2(:,j)=Pn2(:,j)+elems2(:); %distribution of mode 2 over number states
        n1=expect(num1,psi{j});
        n0=expect(num0,psi{j});
        n2=expect(num2,psi{j});
        variance(j)=(expect(num1^2,psi{j})-n1^2)/n1;
        [A0,B0]=eig(full(p0(:,:)));
        b0=diag(B0);
        ex=zeros(1,N0);
        for q=1:N0
           for p=1:N0
              ex(q)=ex(q)+A0(p,q)*conj(A0(p,q))*(p-1);
           end
           expec0(q)=ex(q);
        end
        [A1,B1]=eig(full(p1(:,:)));
     end
  end
  fclose(fid); %close data file (prevents errors)

  %avg. num. of photons in each mode at times tlist
  avg_photon0=photon_num0/ntraj;
  avg_photon1=photon_num1/ntraj;
  avg_photon2=photon_num2/ntraj;
  %probability of mode 0,1,2 being in the ith-# state for the jth elem. in
```

```
%tlist
Pn0=Pn0./ntraj;
Pn1=Pn1./ntraj;
Pn2=Pn2./ntraj;

disp(length(avg_photon0))

figure(Name,Photon Number Statistics);
subplot(4,2,1); plot(taulist, avg_photon0)
title(Mode 0 (Pump))
subplot(4,2,3); plot(taulist, avg_photon1)
title(Mode 1 (Signal))
subplot(4,2,5); plot(taulist, avg_photon2)
title(Mode 2 (Idler))
subplot(4,2,7); plot(taulist, 2*avg_photon0+avg_photon1+avg_photon2)
title(Total Excitations)

subplot(4,2,2); plot(taulist, Pn0(1:3,1:end))
title(Occupation Probabilities)

save(avg_photon0.mat,avg_photon0);
save(avg_photon1.mat,avg_photon1);
save(Pn0.mat,Pn0);
save(Pn1.mat,Pn1);
save(taulist.mat,taulist);

end %ends program----------------------------------
```

Bibliography

[AL02] A. André and M. D. Lukin. Manipulating light pulses via dynamically controlled photonic band gap. *Phys. Rev. Lett.*, 89(14):143602, Sep 2002.

[BQY+08] X.-H. Bao, Y. Qian, J. Yang, H. Zhang, Z.-B. Chen, T. Yang, and J.-W. Pan. Generation of narrow-band polarization-entangled photon pairs for atomic quantum memories. *Phys. Rev. Lett.*, 101(19):190501, Nov 2008.

[BR97] S. M. Barnett and P. M. Radmore. *Methods in Theoretical Quantum Optics.* Oxford Science Publications, 1997.

[BTVac05] A. T. Black, J. K. Thompson, and V. Vuletić. On-demand superradiant conversion of atomic spin gratings into single photons with high efficiency. *Phys. Rev. Lett.*, 95(13):133601, Sep 2005.

[BvL05] S. L. Braunstein and P. van Loock. Quantum information with continuous variables. *Rev. Mod. Phys.*, 77(2):513–577, Jun 2005.

[BZL03] M. Bajcsy, A. S. Zibrov, and M. D. Lukin. Stationary pulses of light in an atomic medium. *Nature*, 426(6967):638, 12 2003.

[CST89] R. A. Campos, B. E. Saleh, and M. C. Teich. Quantum-mechanical lossless beam splitter: SU(2) symmetry and photon statistics. *Phys. Rev. A*, 40(3):1371–1384, Aug 1989.

[Dic54] R. H. Dicke. Coherence in spontaneous radiation processes. *Phys. Rev.*, 93(1):99, Jan 1954.

[DLCZ01] L.-M. Duan, M. D. Lukin, J. I. Cirac, and P. Zoller. Long-distance quantum communication with atomic ensembles and linear optics. *Nature*, 414(6862):413, Nov 2001.

[FL02] M. Fleischhauer and M. D. Lukin. Quantum memory for photons: Dark-state polaritons. *Phys. Rev. A*, 65(2):022314, Jan 2002.

[GAF+07] A. V. Gorshkov, A. André, M. Fleischhauer, A. S. Sørensen, and M. D. Lukin. Universal approach to optimal photon storage in atomic media. *Phys. Rev. Lett.*, 98(12):123601, Mar 2007.

[GALS07] A. V. Gorshkov, A. André, M. D. Lukin, and A. S. Sørensen. Photon storage in Λ -type optically dense atomic media. I. Cavity model. *Phys. Rev. A*, 76(3):033804, Sep 2007.

[HSP10] K. Hammerer, A. S. Sørensen, and E. S. Polzik. Quantum interface between light and atomic ensembles. *Rev. Mod. Phys.*, 82(2):1041–1093, Apr 2010.

[JDB+04] V. Josse, A. Dantan, A. Bramati, M. Pinard, and E. Giacobino. Continuous variable entanglement using cold atoms. *Phys. Rev. Lett.*, 92(12):123601, Mar 2004.

[KC09] A. B. Klimov and S. M. Chumakov. *A Group-Theoretical Approach to Quantum Optics: Models of Atom-Field Interactions.* Wiley, 2009.

[Kim08] H. J. Kimble. The quantum internet. *Nature*, 453(7198):1023, June 2008.

[KWS06] C. E. Kuklewicz, F. N. C. Wong, and J. H. Shapiro. Time-bin-modulated biphotons from cavity-enhanced down-conversion. *Phys. Rev. Lett.*, 97(22):223601, Nov 2006.

[LCS99] N. Lütkenhaus, J. Calsamiglia, and K.-A. Suominen. Bell measurements for teleportation. *Phys. Rev. A*, 59(5):3295–3300, May 1999.

[LFC+01] M. D. Lukin, M. Fleischhauer, R. Cote, L. M. Duan, D. Jaksch, J. I. Cirac, and P. Zoller. Dipole blockade and quantum information processing in mesoscopic atomic ensembles. *Phys. Rev. Lett.*, 87(3):037901, Jun 2001.

[LSSH01] S. Lloyd, M. S. Shahriar, J. H. Shapiro, and P. R. Hemmer. Long Distance, Unconditional Teleportation of Atomic States via Complete Bell State Measurements. *Phys. Rev. Lett.*, 87(16):167903, Sep 2001.

[Luk03] M. D. Lukin. Colloquium: Trapping and manipulating photon states in atomic ensembles. *Rev. Mod. Phys.*, 75(2):457–472, Apr 2003.

[MdVPC08] C. A. Muschik, I. de Vega, D. Porras, and J. I. Cirac. Quantum processing photonic states in optical lattices. *Phys. Rev. Lett.*, 100(6):063601, Feb 2008.

[NB10] P. D. Nation and M. P. Blencowe. The trilinear Hamiltonian: a zero-dimensional model of Hawking radiation from a quantized source. *New Journal of Physics*, 12(9):095013, 2010.

[OSdR+09] C. Ottaviani, C. Simon, H. de Riedmatten, M. Afzelius, B. Lauritzen, N. Sangouard, and N. Gisin. Creating single collective atomic excitations via spontaneous Raman emission in inhomogeneously broadened systems: Beyond the adiabatic approximation. *Phys. Rev. A*, 79(6):063828, Jun 2009.

[RS06] M. Razavi and J. H. Shapiro. Long-distance quantum communication with neutral atoms. *Phys. Rev. A*, 73(4):042303, Apr 2006.

[SdRA+07] C. Simon, H. de Riedmatten, M. Afzelius, N. Sangouard, H. Zbinden, and N. Gisin. Quantum repeaters with photon pair sources and multimode memories. *Phys. Rev. Lett.*, 98(19):190503, May 2007.

[Sha02] J. H. Shapiro. Architectures for long-distance quantum teleportation. *New Journal of Physics*, 4(1):47, 2002.

[Sha08] J. H. Shapiro. 6.453 Quantum Optical Communication Lecture Notes. 2008.

[SKB09] M. Scholz, L. Koch, and O. Benson. Statistics of narrow-band single photons for quantum memories generated by ultrabright cavity-enhanced parametric down-conversion. *Phys. Rev. Lett.*, 102(6):063603, Feb 2009.

[SKUB09] M. Scholz, L. Koch, R. Ullmann, and O. Benson. Single-mode operation of a high-brightness narrow-band single-photon source. *Applied Physics Letters*, 94(20):201105, 2009.

[SSdRG09] N. Sangouard, C. Simon, H. de Riedmatten, and N. Gisin. Quantum repeaters based on atomic ensembles and linear optics. *ArXiv e-prints 0906.2699*, June 2009.

[Ste10] D. A. Steck. *Quantum and Atom Optics.* available online at http://steck.us/teaching (revision 0.2.5, 5 February 2010), 2010.

[STTVac07] J. Simon, H. Tanji, J. K. Thompson, and V. Vuletić. Interfacing collective atomic excitations and single photons. *Phys. Rev. Lett.*, 98(18):183601, May 2007.

[SW00] J. H. Shapiro and N. C. Wong. An ultrabright narrowband source of polarization-entangled photon pairs. *Journal of Optics B: Quantum and Semiclassical Optics*, 2(1):L1, 2000.

[Tan99] S. M. Tan. A computational toolbox for quantum and atomic optics. *Journal of Optics B: Quantum and Semiclassical Optics*, 1(4):424, 1999.

[TGS+09] H. Tanji, S. Ghosh, J. Simon, B. Bloom, and V. Vuletić. Heralded single-magnon quantum memory for photon polarization states. *Phys. Rev. Lett.*, 103(4):043601, Jul 2009.

[TSLVac06] J. K. Thompson, J. Simon, H. Loh, and V. Vuletić. A High-Brightness Source of Narrowband, Identical-Photon Pairs. *Science*, 313(5783):74–77, 2006.

[TYD+10] O. Thomas, Z. L. Yuan, J. F. Dynes, A. W. Sharpe, and A. J. Shields. Efficient photon number detection with silicon avalanche photodiodes. *Applied Physics Letters*, 97(3), 2010. cited By (since 1996) 1.

[WZ82] W. K. Wootters and W. H. Zurek. A single quantum cannot be cloned. *Nature*, 299(5886):802–803, October 1982.